MORPHOLOGICAL AND MAGNETIC CHARACTERIZATION OF ELECTRODEPOSITED MAGNETITE

SHAWN MICHAEL EDWARD CHATMAN

Morphological and Magnetic Characterization of Electrodeposited Magnetite

by

Shawn Michael Edward Chatman

A Thesis Submitted in Partial Fulfilment of
the Requirements for the Degree of

Masters of Science

Department of Physics and Physical Oceanography
Memorial University of Newfoundland

September, 2005

St. John's Newfoundland

Abstract

This thesis describes the synthesis, structure, morphology, and magnetic property relations of electrodeposited magnetite. Thin film magnetite was synthesized on polycrystalline brass or Au/Cr/glass substrates using an aqueous electrodeposition technique. Magnetite formation in electrolytes (containing KCH_3COO and $Fe(SO_4)_2(NH_4)_2$) required temperatures between 60°C and 85°C, and deposition potentials between -0.300 V and 0.575 V or galvanostatic current densities between 50 $\mu A/cm^2$ and 88 $\mu A/cm^2$. Magnetite crystallites had an octahedral habit when grown from electrolytes with low acetate concentrations, and a more rounded morphology when grown from acetate-enriched electrolytes. Magnetic hysteresis studies show that magnetite grown with lower acetate concentrations displays monotonically increasing coercivity (100–300 Oe), and monotonically decreasing squareness (80–35%), with increasing overpotential. In contrast, magnetite grown from acetate-enriched electrolytes had a much lower squareness ($\sim$ 25%) and coercivity ($\sim$ 50 Oe). This evidence suggests that potential and electrolyte composition can be adjusted to change domain behaviour from pseudo-single domain type (for low overpotentials and low acetate concentrations) to multi-domain type (for either high overpotentials or high acetate concentration).

Magnetic hysteresis data also show that an exchange bias is present in samples

containing both magnetite and iron oxide hydroxides. A preliminary study has shown that it is difficult to electrodeposit distinct bilayers of magnetite and the antiferromagnetic iron hydroxide goethite ($\alpha-$FeOOH).

Acknowledgements

I would like to sincerely thank Dr. Kristin Poduska for all the time, effort, and patience during the completion of this thesis. Without her generous contribution this thesis would never have been written.

I would like to thank Adam J. G. Noel for his contribution, as he synthesized some of the samples analyzed here. I would like to thank the following people for instrument time and data collection: Dr. John Shirokoff of the Faculty of Engineering and Applied Science (X-ray diffraction), Dr. Lawrence Thompson and Dr. Martin Lemaire of the Chemistry Department (SQUID magnetometry), Dr. Joe Hodych and Mr. Raymond Patzold of the Department of Earth Sciences (ballistic magnetometer and much advice), and Dr. Ted Monchesky of the Physics Department at Dalhousie University for the use of their XPS and magnetometry facilities. I would also like to thank the following people for letting me use their instruments: Dr. Roger Mason and Mrs. Helen Gillespie of the Department of Earth Sciences for the use of their XRD facilities, and Mrs. Lisa Lee and the Biology Department for the use of their SEM and EDX facilities.

I would like to thank Dr. Todd Andrews and Chris Young of the Department of Physics and Physical Oceanography for their cooperation and work during Brillouin Spectroscopy studies.

I would also like to thank my mother and father for all their patience, time, and help. I would also like to thank my family and friends, inside and out of the Physics Department, for all their help and support.

Contents

1 Introduction **1**

2 Theory **7**
2.1 Electrodeposition 7
2.1.1 Reduction/Oxidation Reactions 7
2.1.2 Metal Oxide Electrodeposition 12
2.2 Magnetism 15
2.2.1 Ferromagnetism 15
2.2.2 Ferrimagnetism 22
2.2.3 Antiferromagnetism 24
2.2.4 Exchange Anisotropy 24

3 Experimental Methods **29**
3.1 Synthesis 29
3.1.1 Apparatus 29
3.1.2 Procedure 32
3.2 Analysis Techniques 34
3.2.1 X-Ray Diffraction 34
3.2.2 Scanning Electron Microscopy 43
3.2.3 Energy Dispersive X-Ray Analysis 45
3.2.4 Magnetometry 47
3.2.5 Atomic Force Microscopy 48

4 Influencing Morphology and Magnetism **50**
4.1 Confirming Phase Composition 51
4.2 Tuning Structure With Applied Potential 55
4.3 Modifying Electrolyte to Affect Deposition Kinetics 57
4.3.1 Ammonium Concentration 58
4.3.2 Acetate Concentration 59
4.4 Magnetic Characterization 63

4.4.1 Verwey Transition 63
4.4.2 Saturation Magnetization 65
4.4.3 Hysteresis 66

5 Electrodeposited Iron Oxide Composite Materials 70
5.1 Hysteresis Loop Shifts 70
5.2 Preparation of Multi-Phase Deposits 72

6 Conclusions 76
6.1 Conclusions 76
6.2 Future Studies 79

Bibliography 84

List of Tables

3.1 Standard XRD diffraction pattern of magnetite, JCPDS #19 – 0629. Intensity is given as a percentage of the largest peak (311) [63]. . . . 41

5.1 Summary of deposition conditions for two-phase exchange biased samples. Goethite deposition occurred at −0.300 V (varying times), while magnetite deposition occurred at −0.375 V (20 minutes). The electrolyte, containing 0.01 M $Fe(SO_4)_2(NH_4)_2{\cdot}6H_2O$ + 0.04 M KCH_3COOH, and was maintained at 80°C. 75

List of Figures

1.1 The inverse spinel crystal structure of Fe_3O_4, magnetite. Oxygen sites can be seen in red, tetrahedral Fe sites in green, and octahedral Fe sites in grey. 3

2.1 Cyclic voltammogram (CV) of the gold/gold oxide redox couple. This CV shows the current response recorded when a potential is swept across a polycrystalline Au working electrode in $\sim$ 0.01 M H_2SO_4 (pH 1.7) at 50 mV/s. The broad peak above 1.0 V is due to the oxidation of gold at the surface of the working electrode. The peak near 0.8 V is due to the reduction of the gold oxide. 11

2.2 A simplified version of Pourbaix's calculated phase stability diagram for iron ions in water at 25°C [29]. 15

2.3 A schematic representation of domains in a ferromagnetic material. The arrows show the magnetization direction in each different domain. Modified from Blundell [30]. 17

2.4 This diagram shows the same domains seen in Figure 2.3 under the influence of an externally applied magnetic field, H. Notice the unidirectional orientation. 18

2.5 A schematic representation of a hysteresis loop in which remanent magnetization, saturation magnetization, and coercivity are labeled. Notice that increased remanence increases the squareness of the loop. . . 19

2.6 Schematic diagram of the typical hysteresis response exhibited by single domain, multi-domain, and pseudo-single domain crystallites. 20

2.7 Spin cancellation associated with the Fe^{3+} ions in the octahedral and tetrahedral sites. The result is a ferrimagnetic material in which the net magnetic response can be attributed solely to the spin of the Fe^{2+} ions in the octahedral sites. Adapted from Kittel [8] 23

2.8 Schematic diagram of a system containing both ferromagnetic and antiferromagnetic materials under an applied magnetic field, H, and cooled/grown below the Néel temperature. Notice that the axis of magnetization is the same for both materials. 25
2.9 Schematic diagram of a schematic hysteresis loop displaying exchange bias. Notice the shift of the loop along the horizontal applied field (H) axis. The exchange field, H_E, is the average of coercivities H_{c1} and H_{c2}. 27

3.1 Schematic diagram of the setup used for the electrodeposition of magnetite during this thesis. This is a practical adaptation of a traditional setup, as described by Bard and Faulkner [20] 31
3.2 Schematic illustration of the Von Laue reradiator formulation. Adapted from Ashcroft and Mermin [62]. 35
3.3 Two-dimensional representation of the Ewald construct sphere. The two vectors, **k** and **k′**, satisfy the Laue condition and would lead to constructive interference. Adapted from Ashcroft and Mermin [62]. . 37
3.4 Diagram showing the equivalence of the Laue rereadiator formulation of X-ray scattering with reflection from a Bragg plane. The dashed line represents a Bragg plane perpendicular to **K**, **k**, and **k′**. 39
3.5 Diagram showing a typical X-ray diffractometer. 40
3.6 Scanning electron micrograph of the brass shimstock used as a substrate for the deposition of magnetite. The rolling direction is indicated in this image. 44
3.7 A representative energy dispersive X-ray (EDX) energy spectrum. Peaks from copper and zinc peaks in this spectra are due to the brass substrate, while gold peaks are due to the evaporated gold used to increase the conductivity of the films for SEM imaging. The iron peaks are due to the deposited magnetite. Oxygen is not seen here because its atomic number is too low to be detected by our system. 46

4.1 Indexed XRD diffraction pattern from a thin film of magnetite prepared by potentiostatic deposition at −0.375 V. Peaks resulting from the brass substrate are marked with an asterisk (*). The observed Bragg reflections are excellent matches with those expected for magnetite, JCPDS #19-0629 [63]. 53
4.2 Applied deposition potential *vs.* time for a sample prepared galvanostatically at 50 $\mu A/cm^2$. Within the first 15 seconds of deposition, the applied potential stabilizes to a potential at which magnetite is electrodeposited, and no significant variation in potential is observed over $15 - 90$ minutes of deposition. 53

4.3 Scanning electron micrographs of magnetite deposited potentiostatically (−0.350 V for 30 minutes) and galvanostatically (+50 μA for 30 minutes). Octahedral crystallite habits, circled in red, are observed in samples prepared by either method. Energy dispersive X-ray analysis (EDX) was carried out on these samples in order to verify that no contaminants were present. 54
4.4 Linear sweep voltammogram of 0.01 M $Fe(SO_4)_2(NH_4)_2 \cdot 6H_2O$ + 0.04 M KCH_3COOH at 1 mV/s. The circled center region indicates the potentials at which magnetite can be deposited. In the region more negative than these potentials, no deposit is seen. In the region more positive than this, goethite (γ-FeOOH) forms. 57
4.5 Scanning electron micrograph of magnetite deposited potentiostatically (−0.475 V for 25 minutes) from electrolyte containing 2.0 M acetate. More rounded crystallite habits are observed in samples prepared from electrolytes with higher acetate concentrations. 62
4.6 Indexed XRD diffraction pattern from a thin film of magnetite prepared by potentiostatic deposition at −0.475 V from an acetate-enriched electrolyte. Peaks resulting from the gold substrate are marked with an asterisk (*). The observed Bragg reflections are excellent matches with those expected for magnetite, JCPDS #19-0629 [63]. 62
4.7 The temperature dependence of the saturation magnetization of a sample of electrodeposited magnetite (deposited potentiostatically at −0.375 V for 30 minutes). The magnetization was recorded after the sample was cooled both without a magnetic field (ZFC) and in a magnetic field (FC). The magnetization reaches a maximum at the Verwey temperature (115 K). 64
4.8 Representative magnetic hysteresis loops obtained from potentiostatically-deposited samples at −0.325 V (a), −0.350 V (b), and −0.425 V (c). The loops shown in (a) and (b) are from deposits prepared with electrolytes with 0.04 M acetate, while the loop in (c) is from a deposit prepared from an electrolyte containing 2 M acetate. 67
4.9 Magnetic coercivity plotted as a function of overpotential shows a strong trend of increasing coercivity with increasing overpotential. All coercivity data were obtained with a field applied in the in-plane orientation. The overpotentials are calculated relative to the pH-dependent Nernst reversible potential for the Fe^{2+}/Fe^{3+} redox reaction (-0.630 V *vs.* Ag/AgCl). 68
4.10 Hysteresis loop squareness plotted as a function of overpotential shows a strong trend of decreasing squareness with increasing overpotential. The overpotentials are calculated relative to the pH-dependent Nernst reversible potential for the Fe^{2+}/Fe^{3+} redox reaction (-0.630 V *vs.* Ag/AgCl). 69

5.1 This hysteresis loop shows clear exchange bias with a positive shift along the x (applied field) axis of about 10%. 72
5.2 Indexed XRD pattern of a sample potentiostatically deposited at -0.300 V for 30 minutes. Peaks from the gold substrate are marked with an asterisk(*). This diffraction pattern is an excellent match with that of goethite ($\gamma-$FeOOH), JCPDS #29-0713 [63]. 73
5.3 SEM micrograph displaying a mixed phase deposit where both goethite (diamond-shaped) and magnetite (octahedral) can be seen. This sample was prepared galvanostatically at 50 μA/cm^2 for 45 minutes. . . . 74

Chapter 1

Introduction

In the race to make faster, cheaper, and better microelectronic devices, such as nonvolatile random access memory (RAM) and high-density recordable media [1], researchers have been reviewing the electronic, magnetic, and mechanical properties of many types of materials. Magnetite (Fe_3O_4), as a half-metal, has garnered some of this attention [2, 3]. Half-metals have only one occupied spin band at the Fermi level, so conduction is completely spin dependent [4, 5]. This characteristic is of use in micro-electronic components such as spin valves and giant magnetoresistive (GMR) devices where a magnetic field is used to control the flow of electrons through their intrinsic spin. This thesis describes the synthesis, morphological attributes, and magnetic properties of magnetite prepared by electrochemical deposition.

Known historically as lodestone, magnetite is a ferrite material that has long been the subject of materials science research [6]. Ferrites are iron oxide based materials

with the chemical formula $MO{\cdot}Fe_2O_3$, where M is the 2+ ion Fe, Ni, Co, Cu, Zn, Mg, Pb, Cd, and Sn.[1] Magnetite has the cubic inverse spinel structure (space group $Fd\bar{3}m$), which is characterized by 32 cubic closed packed sites per unit cell with 24 interstitial sites (8 tetrahedral and 16 octahedral). In magnetite, the cubic closed packed sites are occupied by oxygen atoms, while the tetrahedral sites are filled with Fe^{3+} ions and the octahedral sites accommodate Fe^{2+} and Fe^{3+} ions, as shown in Figure 1.1 [8]. This mixture of 2+ and 3+ ions allows magnetite to exhibit its interesting magnetic and electronic properties. Based solely on exchange interactions within and between the sublattices of magnetite's structure, an antiparallel spin alignment would be expected. However, there exists a parallel alignment within each sublattice, and an antiparallel alignment between sublattices. In essence, the spins of the Fe^{3+} ions in the octahedral site cancel out the antiparallel spins of the 3+ ions in the tetrahedral sites. Consequently, the spins of the Fe^{2+} ions in the octahedral sites are the only ones that contribute to the net magnetization of magnetite. This results in a net ferrimagnetic moment as well as spin polarization at the Fermi level [1].

Traditionally, thin film magnetite has been synthesized with ultrahigh vacuum (UHV) techniques which typically involve high temperature deposition and annealing. Examples of such UHV techniques include laser ablation [9], electron beam evaporation [10], inductive melting [11], and molecular beam epitaxy [12]. Collectively, these methods can be applied to a vast range of elements and compounds,

[1] If sufficient crystal lattice vacancies are present to maintain the charge balance, the 3+ ions Co, Mn, Cr, Al, V, and Mo can be substituted for M. This is also true for the 4+ ions V, Ti, Mo, and Sn, as well as the Mo^{5+} ion [7].

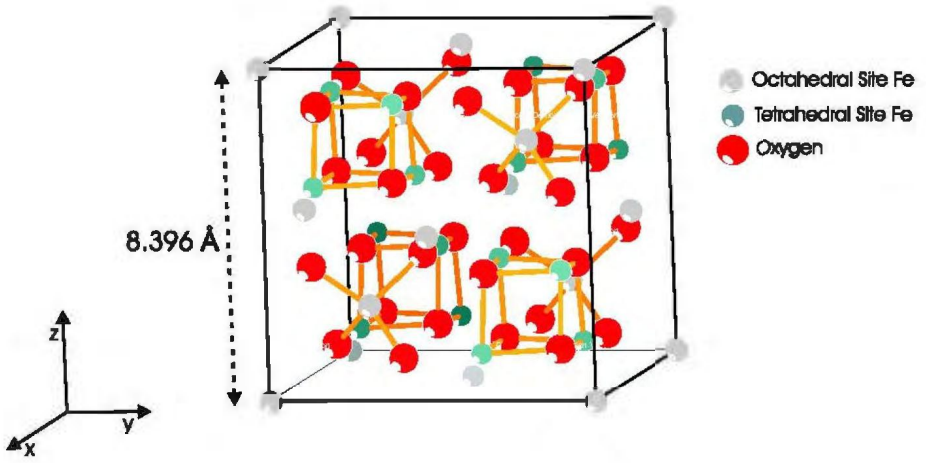

Figure 1.1: The inverse spinel crystal structure of Fe_3O_4, magnetite. Oxygen sites can be seen in red, tetrahedral Fe sites in green, and octahedral Fe sites in grey.

and they can yield very high sample purities. However, instrumentation required for UHV sample preparation is typically very expensive to purchase and operate. Along with high costs, films formed in UHV cannot be deposited upon complex substrate morphologies due to shadowing, and they can have non-uniform thicknesses over large areas due to the directional plumes inherent in laser beam ablation and molecular beam epitaxy systems.

This thesis focuses on magnetite films prepared by electrodeposition, a low-cost, low-temperature synthesis technique that requires no annealing. Electrodeposition uses electron transfer to form deposits, usually of metals and metal oxides, on the surface of a conducting substrate (electrode). By using high purity reagents and ultrapure water, electrodeposition can yield very high purity samples using depositions

near room temperature and without annealing. This is an important advantage of electrodeposition, since many of the substrates used in microelectronics decompose at high temperatures. GaAs and Si become unstable at $\sim 500°C$ and $\sim 900°C$, respectively, so techniques which require high synthesis temperatures or annealing temperatures to form magnetite are not feasible. Thus, electrodeposition's low-temperature sample preparation is a major advantage over techniques that require high temperature synthesis or annealing.

Cost and temperature are not the only attributes of electrodeposited magnetite. Electrodeposition also has many adjustable parameters, similar to UHV techniques, including substrate type, deposition potential, and electrolyte composition. Furthermore, it has been found that film crystallinity, grain size, and grain orientation are some of the characteristics that can be controlled by varying deposition conditions such as deposition potential, temperature, and electrolyte pH [13, 14, 15, 16]. Previous studies into the electrodeposition of magnetite has been mainly undertaken by two research groups. Jay A. Switzer's research group (University of Missouri-Rolla) has focused on the epitaxial electrodeposition of magnetite onto single crystal substrates, and the magnetoresistance of such films [2, 3]. Masanori Abe's group (Tokyo Institute of Technology) has studied the bulk-like properties of electrodeposited thin films of magnetite [7, 17, 18]. Abe's group has created a body of work on electrodeposited magnetite focused on the effects of synthesis conditions on deposition rate, crystallinity, and saturation magnetization, while Switzer's group has investigated

the effects of magnetite deposition on single crystalline substrates and has done preliminary investigations of magnetoresistance. However, device applications will also require studies into the sensitivity of magnetite's hysteresis response, which is the subject of this thesis.

As with any technique, electrodeposition does have some disadvantages. There is a possibility of side reactions occurring that could be detrimental to electrodeposition, such as the *in situ* formation of other iron species while attempting magnetite deposition [18], or fouling of electrodes. Overall, the advantage of using a low cost, low temperature technique to deposit magnetite can outweigh the disadvantages. Consequently, electrodeposition has the potential to be a viable option in the synthesis of thin film magnetite.

The goal of this thesis is to characterize the magnetic properties of magnetite synthesized electrochemically on polycrystalline substrates. Specifically, the effect of film morphology on magnetic response will be explored. A study of the influence of grain size, morphology, and boundary interactions on the magnetic response of thin film magnetite is particularly important to linking deposition conditions with magnetic responses favourable to spintronic device applications. As well, this investigation was performed on polycrystalline substrates so that the reduced cost of such substrates can be weighed against any associated adverse influence due to such substrates. The electrosynthesis of magnetite could offer an economical option for preparing thin film spintronic devices. Studying the relation between deposition conditions, film

morphology, and magnetic response is the first step towards controlled tailoring of film properties. This thesis will first focus on identifying viable electrodeposition conditions for magnetite, including applied potential/current, pH, ionic species, and deposition temperature. Next, this thesis explores the relations between these deposition conditions and the resulting morphologies and magnetic responses of the electrodeposits. In particular, this thesis work relates hysteresis loop squareness and coercivity with specific deposition conditions and morphologies. These relations show a link between the electrolyte composition and/or applied potential and the magnetic domain structure of electrodeposited samples. This correlated study of the synthesis, morphology, and magnetic properties of thin film magnetite lays a solid foundation that could lead to a more in depth analysis of electrodeposited magnetite for spintronic applications. The ability to tailor the magnetic and electronic properties of a material is valuable to the high-technology industry, where the reliable tailoring of materials is essential to manufacturing high quality microelectronic components.

Chapter 2

Theory

While the magnetic study of thin ferromagnetic films is firmly rooted in the physics of magnetic materials, other areas of science must be employed to fully analyze the synthesis-structure-property relations. The study of electrodeposited magnetite is no exception to this. Not only were theories regarding magnetism in thin films utilized in this study, but the theories behind electrodeposition and metal oxide formation were also considered.

2.1 Electrodeposition

2.1.1 Reduction/Oxidation Reactions

The electrochemical synthesis of a material relies on an intimate link between electron transfer and crystallite formation. This transfer of electrons occurs at the surface

of an electrode submersed in an electrolyte. A major portion of the current response in such reactions is due to the oxidation or reduction of an active species within a solution, which is typically proportional to the concentration of the active species within solution [19]. The type of reactions characteristically involved in electrochemical synthesis are reduction/oxidation (redox) reactions. The reduction or oxidation of a chemical species is defined by whether said species gains or loses electrons in the reaction, respectively. Such reactions can be written as a redox couple,

$$\mathrm{O} + ne^- \rightleftarrows \mathrm{R}, \tag{2.1}$$

where O is the oxidized species, R is the reduced species, and n is the number of electrons transferred per reaction. Each redox reaction has a standard potential, E°, that dictates the potential required for electron transfer. At potentials more negative than E°, the reduction of O is more favourable (reductive reaction), while at potentials more positive than E°, the oxidation of R is more favourable (oxidative reaction). Reactions that follow this rule are called faradaic processes [19, 20].

The standard potential of an electrochemical reaction is measured according to the potential difference between the working electrode, at which the reaction occurs, and a reference electrode. In the literature, many authors report standard potentials against the standard hydrogen electrode (SHE), which is the standard potential of the redox reaction of hydrogen gas and H^+. The SHE is the accepted benchmark for reference electrodes. Other reference electrodes, such as the Ag/AgCl electrode,

are measured relative to this. This thesis will report against the Ag/AgCl potential unless otherwise noted (an Ag/AgCl reference electrode is +0.1767 V *vs.* SHE at 80°C [21]).

In real systems, the potential which defines oxidation and reduction can shift from E°, depending on the concentrations of the active species in solution. The Nernst equation quantifies this shift:

$$E = E^{\circ} + \frac{\mathrm{R}T}{nF} \ln \frac{C_{\mathrm{O}}(0,t)}{C_{\mathrm{R}}(0,t)}. \tag{2.2}$$

Here R is the universal gas constant (8.314 $\mathrm{JK^{-1}mol^{-1}}$), T is the temperature in Kelvin, and F is the Faraday constant (94,487 Coulombs). $C_{\mathrm{O}}(0,t)$ and $C_{\mathrm{R}}(0,t)$ are the concentrations of oxidized and reduced species at the surface of the electrode, respectively. Notice that if $C_{\mathrm{O}}(0,t)$ and $C_{\mathrm{R}}(0,t)$ are equal, the Nernst potential will equal the standard potential.

A straightforward example of a redox process is the reduction-oxidation of iron metal (Fe^0) and the iron ion (Fe^{2+}), for which the standard potential is −0.440 V *vs.* SHE [22].

$$\mathrm{Fe}^{2+}_{(\mathrm{aq})} + 2e^- \rightleftarrows \mathrm{Fe}_{(\mathrm{s})} \tag{2.3}$$

At potentials more negative than −0.440 V *vs.* SHE, the formation of the reduced species (Fe^0) is more favourable, while at potentials more positive than −0.440 V *vs.* SHE, the formation of the oxidized species (Fe^{2+}) is more favourable.

If a redox reaction occurs at a high enough rate that it can be considered in thermodynamic equilibrium as the potential is swept, it is considered a reversible reaction. Such a system can theoretically be reduced and oxidized an infinite number of times without adverse affect (no loss of O or R). Cyclic voltammograms (CV) can be used to study redox reactions more extensively. These plots relate response current to the applied potential as the working electrode potential is ramped linearly between two potentials. Changes in current indicate a surface or electrolyte reaction. Current peaks can be seen in the CV shown in Figure 2.1, wherein the positive (anodic) current peak is indicative of gold oxidation at the surface of the working electrode, while the negative (cathodic) current peak is due to the reduction of the formed oxide, Au_2O_3, back to Au. Because gold oxidizes at relatively positive potentials, and is inert at more negative potentials where metal redox reactions of interest take place, it is widely used as a working or counter electrode in electrodeposition experiments. Notice that the oxidation peak for this system is broader than the reduction peak. This is due to the oxidation of gold occurring at different crystal faces of the polycrystalline working electrode. The high scan speed of the cyclic voltammogram (50 mV/s) can also broaden both reduction and oxidation current peaks.

Along with peak position, CVs can also be used to determine the amount of electron transfer during a given process by calculating the area under a current peak [19, 20]. In Figure 2.1, the area under the gold reduction peak will equal the area under the gold oxidation peak because the same number of electrons transfered in

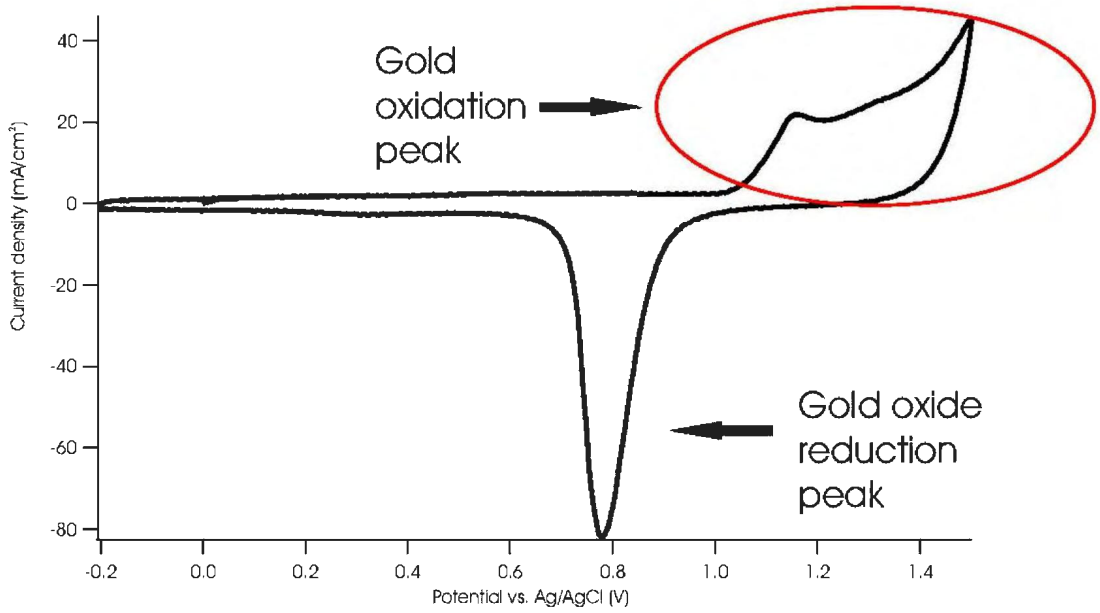

Figure 2.1: Cyclic voltammogram (CV) of the gold/gold oxide redox couple. This CV shows the current response recorded when a potential is swept across a polycrystalline Au working electrode in $\sim$ 0.01 M H_2SO_4 (pH 1.7) at 50 mV/s. The broad peak above 1.0 V is due to the oxidation of gold at the surface of the working electrode. The peak near 0.8 V is due to the reduction of the gold oxide.

the oxidation reaction will be transfered back in the reduction reaction. If multiple processes occur at a given potential, extracting accurate values of transferred charge can be complicated. For example, the evolution of hydrogen in aqueous solutions due to water hydrolysis occurs at -0.828 V SHE, which would interfere with accurate charge counting during iron metal deposition [22].

2.1.2 Metal Oxide Electrodeposition

In contrast to simple redox, there are other electrochemical reactions of interest that occur during electrodeposition, and are much more complicated to quantify. For example, metal oxide deposition can involve the formation of *in situ* intermediate species. The electrochemical synthesis of metal oxides can be achieved by several different techniques, such as electromigration of reactant species, electrolysis of fused salts, electrogeneration of base by cathodic reduction, alternate current synthesis, or anodic oxidation. The first technique, electromigration of reactant species, utilizes a potential difference between a counter electrode and a host lattice (working electrode) to intercalate guest ions into the lattice to form metal oxides [23]. Electrolysis of fused salts involves the anodic oxidation or cathodic reduction of metal oxide containing low-melting salts at the surface of an electrode to make single crystal metal oxides. These single crystals can be collected after the electrolyte has been washed away. Cathodic reduction requires the production of a basic species at the surface of an electrode to form *in situ* metal ions and metal complexes in solution or at the surface

of the working electrode. Therese *et al.* previously reviewed this technique and report many of the metal oxides that can be synthesized and some of their applications [13]. Switzer *et al.* have used this technique previously to synthesize ceric oxide powders [24]. Therese *et al.* have also reviewed alternate current techniques, which use galvanostatic currents stepped between two separate values to deposit multi-layer systems. To date, only Switzer's group has used this technique successfully, using stepped currents to electrosynthesize compositionally-modulated thallium lead oxide thin film superlattices [25]. The final technique, anodic oxidation, is the most relevant to our study of electrodeposited magnetite.

During anodic oxidation synthesis, a metal or lower oxidation metal ion is oxidized to a higher oxidation state using an anodic current. The pH of the aqueous electrolyte used for this type of synthesis is very important. The lower oxidation state must be stable while the higher oxidation state will form a hydroxide. This technique is particularly well suited to depositing ferrites, such as magnetite [2, 3, 18]. Abe and Tamaura pioneered the use of anodic oxidation to electrosynthesize thin film ferrites in the early 1980's [17], but the exact mechanism of magnetite formation is still not completely understood. To form magnetite, Fe^{2+} and Fe^{3+} are hydrolyzed to $FeOH^{+}$ and $FeOH^{2+}$ adsorbed on the surface of the working electrode. Anodic current is then used as an oxidizing agent to convert some of the $FeOH^{+}$ to $FeOH^{2+}$ at the surface of the electrode, leading to magnetite formation:

$$2FeOH^{2+} + FeOH^{+} + OH^{-} \rightarrow (Fe^{3+}, Fe^{2+})_3O_4 + 4H^{+} \quad (2.4)$$

It is easy to see that this reaction is not a simple redox reaction, but rather is a series of reactions assisted by the anodic oxidation of Fe^{2+} to Fe^{3+}. Consequently, once magnetite has been deposited, the Fe^{3+} within the deposited thin film cannot be reduced back to Fe^{2+} merely by changing the potential. This proposed mechanism has not been confirmed; there is no evidence of the formation of the $FeOH^{+}$ and $FeOH^{2+}$ precursors. However, this synthesis approach has been used recently to form high quality magnetite electrodeposits utilizing flow through cells [18, 26], spray-spin coating [17, 27] or epitaxially using single crystal substrates [2, 3, 28].

The choices of potential and temperature ranges for magnetite electrodeposition explored in this thesis were guided by the theoretical thermodynamic calculations of the stability of magnetite and iron ions in water. The phase stability of magnetite and other phases of iron oxide can be found in a calculated pH-potential phase stability (Pourbaix) diagram. A simplified version of Pourbaix's diagram for iron and its oxides and hydroxides at 25°C can be seen in Figure 2.2. Magnetite is stable over the potential range −0.500 V to −0.300 V *vs.* Ag/AgCl, and the pH range 5.5-8.5 at 25°C. Since this Pourbaix phase plot is based only on thermodynamic phase stability of iron ions in water, the actual pH and potential regions for magnetite stability can be altered with the addition of buffering and/or complexing agents (such as potassium acetate), to the system.

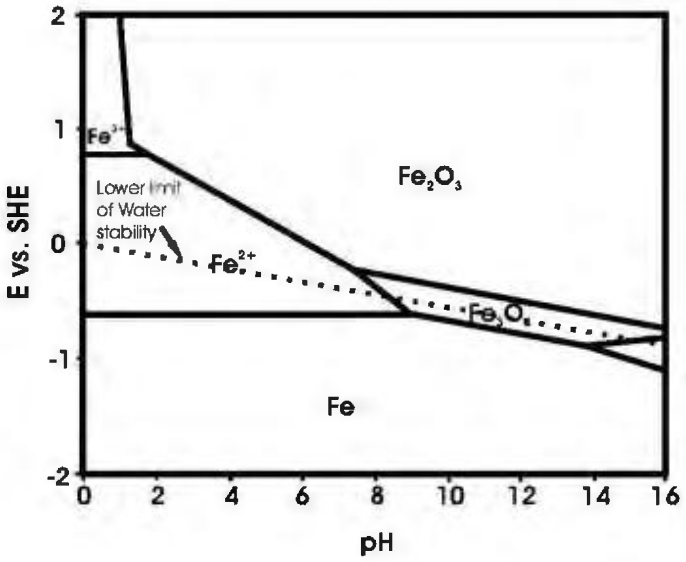

Figure 2.2: A simplified version of Pourbaix's calculated phase stability diagram for iron ions in water at 25°C [29].

2.2 Magnetism

2.2.1 Ferromagnetism

An important characteristic of magnetite is its ability to retain long-range magnetic order after being subjected to an externally-applied magnetic field; magnetite is a ferrimagnetic material. Ferrimagnetism is closely linked with ferromagetism, the property that allows static objects to produce spontaneous intrinsic magnetic fields [30]. This means that ferromagnets remain magnetized once magnetized by an external magnetic field, suggesting an intrinsic ordering of magnetic moments. This long range ordering is due to both the short-range exchange interaction and the long-range magnetic dipolar interaction between spins within a material. The exchange inter-

action can be treated as a magnetic field and is called the exchange field, B_E. The exchange coupling in ferromagnetic materials may be as high as 10^3 T and falls off exponentially with distance, while the dipolar coupling strength is typically a thousand times less than this but falls off with the inverse cube of distance [8, 30].

A domain consists of a localized area of a material wherein the spins of unpaired electrons are all aligned with their neighbours. The existence of domains is strongly related to the relative strengths and ranges of the exchange and dipolar interactions. It is costly in dipolar energy for a material to be uniformly magnetized. To reduce dipolar energy, it is favourable for a ferromagnetic material to form domains with different spin orientations. While this will increase the exchange energy at the domain boundaries (domain walls), this is only applicable over a very short length scale near the boundaries. The dipolar energy, on the other hand, will decrease across the whole material, thereby reducing the total energy of the system. A two-dimensional representation of domains in a ferromagnetic material can be seen in Figure 2.3 [31].

When an external magnetic field is applied to a ferromagnetic material, it becomes energetically favourable for more of the unpaired electron spins to align with the applied field, as shown in Figure 2.4. As a result, the domains that are aligned with the external field will reduce the overall energy of the system. An alignment transition occurs at the domain walls; domains that are the most closely aligned with the applied field will expand as the spins from the edges of neighbouring domains align. The result is domain wall motion as aligned domains grow and un-aligned domains

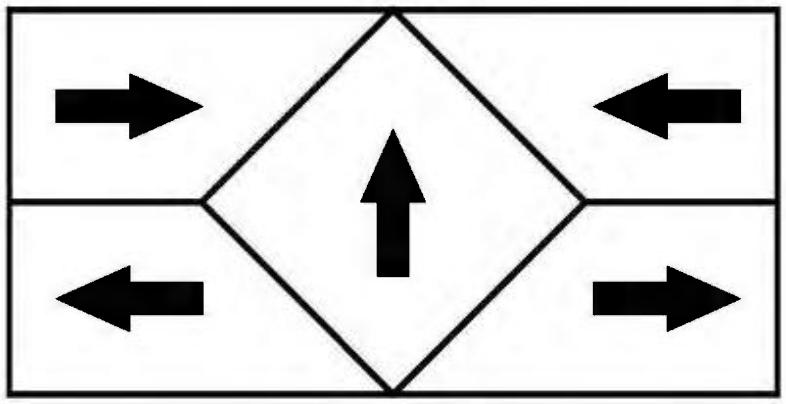

Figure 2.3: A schematic representation of domains in a ferromagnetic material. The arrows show the magnetization direction in each different domain. Modified from Blundell [30].

shrink. Domain wall motion in ferromagnets typically occurs in small discontinuous steps (Barkhousen effect) due to domain wall pinning by strains, surfaces, and crystal impurities [30].

The net magnetization of a ferromagnetic material is dependent upon the strength of the applied magnetic field: the magnetization will increase in an increasing magnetic field until a limiting magnetization is reached. At this limiting magnetization (saturation), all spins are aligned with the applied field.

Ferromagnetic behaviour is seen only at temperatures below the material's ferromagnetic ordering temperature (Curie), T_C. Above this temperature, thermal excitations within the material are great enough to disrupt the long-range alignment of the spins. Consequently, a ferromagnetic material will behave as a paramagnetic material at temperatures above T_C [30, 31]. The maximum saturation magnetization of a ferromagnet decreases as temperature increases approaching T_C. This temper-

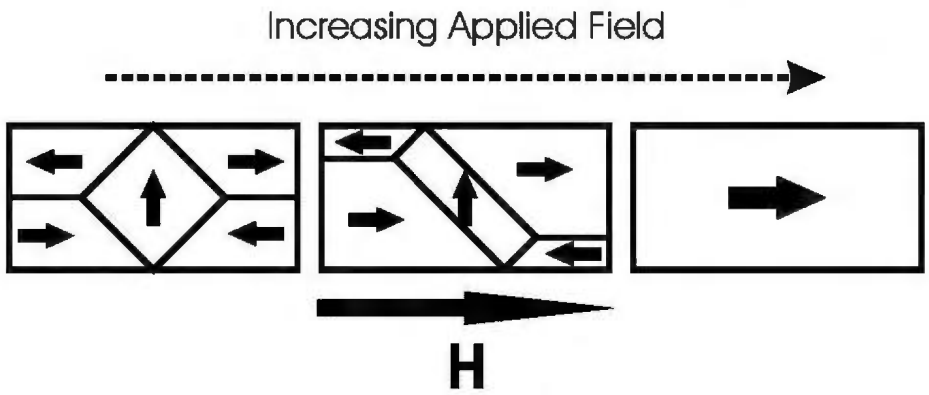

Figure 2.4: This diagram shows the same domains seen in Figure 2.3 under the influence of an externally applied magnetic field, H. Notice the unidirectional orientation.

ature dependence follows the Curie-Weiss law, Eqn 2.5, which relates the magnetic susceptibility (χ_m), the ability to be magnetized by an applied field, of a material to temperature.

$$\mathbf{M} = \chi_m \mathbf{H} = \frac{C}{T_C - T}\mathbf{H}. \tag{2.5}$$

Here C is the curie constant, $\mathbf{M}$ is the sample magnetization, $\mathbf{H}$ is the applied magnetic field.

While saturation magnetization is an intrinsic property of a ferromagnetic material, other magnetic characteristics such as coercivity and remanent magnetization can be strongly affected by defects within the material. Once an applied magnetic field is removed, a ferromagnetic material still retains a "memory" of its fully magnetized state. However, this remaining (remanent) magnetization will often be lower than the saturation magnetization. Thermal energy can randomize some spins, nu-

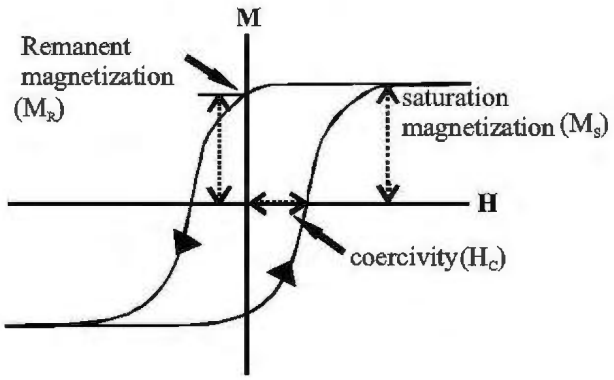

Figure 2.5: A schematic representation of a hysteresis loop in which remanent magnetization, saturation magnetization, and coercivity are labeled. Notice that increased remanence increases the squareness of the loop.

cleating new domains causing domain wall motion. Since movement of domain walls will not always be a smooth process due to the Barkhousen effect, there will be some remanent magnetization even with zero applied field. Coercivity is the amount of reverse applied field required to bring the net magnetization back to zero [30, 32].

The analysis of ferromagnetic materials often involves the study of hysteresis loops, which are plots of a material's magnetic response in a sweeping applied field, as shown in Figure 2.5. Saturation magnetization (M_S), remanent magnetization (M_R), and coercivity (H_C) are indicated on this plot. The analysis of hysteresis loops is an important tool in determining the domain structure of a material. Figure 2.6 shows schematically the link between loop shape and domain behaviour type. When dealing with polycrystalline materials, there can exist three kinds of domain structures. Crys-

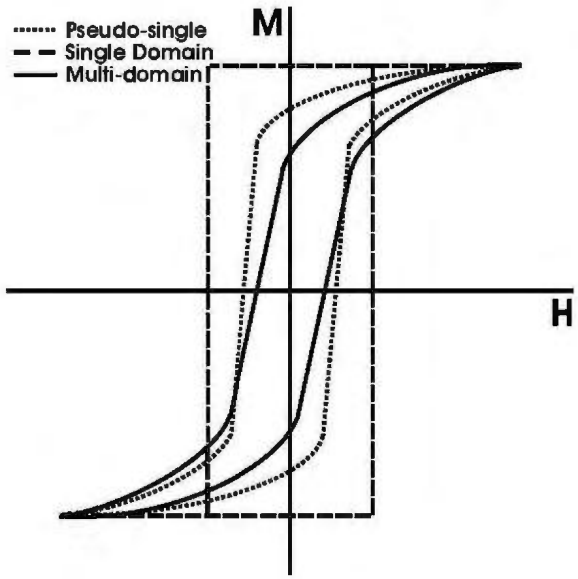

Figure 2.6: Schematic diagram of the typical hysteresis response exhibited by single domain, multi-domain, and pseudo-single domain crystallites.

tallites that contain only one domain (single-domain crystallites) are typically seen when the grain size is too small to accommodate domain walls [33]. In magnetite, this type of domain structure is often seen with a grain size of 80 nm and below. Single-domain crystallites display high squareness and high coercivity because their larger domain size require higher applied fields to magnetize and demagnetize. Since there is only one domain per crystallite in these types of crystallites, domain wall motion does not occur. The magnetization will remain in its original direction until the strength of the applied field is large enough to flip the domain orientation. In a hysteresis loop this would look like a rectangle, as shown in Figure 2.6

Multi-domain crystallites are typically seen in materials with larger grain sizes, typically > 20 μm in magnetite. Multi-domain crystallites show lower coercivities

because the magnetization of these materials utilizes domain wall motion to align domains. Compared to a single domain crystallite, it is energetically easier for the domain walls to shift than it is for a whole domain to flip. Consequently, it requires less energy to demagnetize material composed of multi-domain crystallites. Resultingly, thermal excitation can disrupt domain order more easily, which leads to lower remanent magnetization and squareness in multi-domain materials.

The third domain structure, pseudo-single domain, shows a mixture of single-domain and multi-domain magnetic responses, and occurs in multi-domain crystallites near the lower size limit ($0.1 - 20$ μm in magnetite) [34]. In such materials, multiple domains act in unison to simulate the remanence characteristics of single-domain crystallites, but display the low coercivity of multi-domain crystallites. This is due to the fact that it is still energetically favourable to have domain walls to lower the dipolar energy, but since the crystallites are smaller than multi-domain crystallites, the reduction of dipolar energy does not outweigh the exchange coupling.

While it is possible to infer magnetic domain structure from hysteresis behaviour, domains can also be observed directly. The traditional method to observe domains is the Bitter method, which involves observing ferromagnetic colloids that gather at domain walls with optical microscopy or with the unaided eye [35]. More modern experimental techniques for direct domain observation include synchrotron-radiation X-ray topography [36], Kerr effect microscopy [37], and scanning magnetic force microscopy (MFM) [38, 39]. MFM and Kerr effect microscopy applied to magnetite will

be addressed in Chapter 2 and Chapter 6, respectively.

2.2.2 Ferrimagnetism

To explore the difference between ferromagnetic and ferrimagnetic materials, the geometric arrangements of atoms with unpaired electron spin must be considered. Magnetite is a ferrite with an inverse spinel structure containing both Fe^{3+} and Fe^{2+} ions, with spin states of $S = \frac{5}{2}$ and $S = 2$, respectively. If it is assumed that all the ions in the formula unit of magnetite contributed to the magnetite moment (two Fe^{3+} ions and one Fe^{2+} ion), then the total spin magnetic moment would be 14 Bohr magnetons[1]. (μ_B) per formula unit. Magnetometer studies have shown that the actual spin magnetic moment per formula unit for magnetite to be 4.07 μ_B [41], which corresponds to the contribution by only the Fe^{2+} ions [8, 40, 42]. It turns out that there is a structural reason for only observing the Fe^{2+} contribution, and it is directly related to magnetite's designation as a ferrimagnetic material.

Ferrimagnetism stems from the uneven magnitudes of antiparallel aligned magnetic moments between the sublattices of a crystal structure. In magnetite, as mentioned in Chapter 1, there are 24 iron ions per primitive unit cell with eight Fe^{3+} ions in the tetrahedral sites and eight in the octahedral sites. These two sets of Fe^{3+} ions have magnetic moments that are aligned antiparallel, which results in a net zero con-

[1]The Bohr magneton is a constant that almost equals the spin magnetic moment of an unpaired electron [8]. While intuitively it seems that the number of Bohr magnetons should be integral, this is often not the case. Non-integral spin magnetic moment values can be due to other influences such as spin-orbit interaction contributing a magnetic moment, as in the case of magnetite, or conduction electron magnetization from the paramagnetic nucleus of an atom [8, 40]

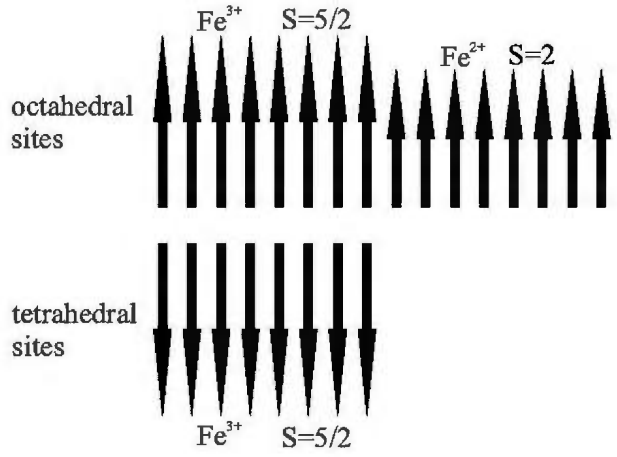

Figure 2.7: Spin cancellation associated with the Fe^{3+} ions in the octahedral and tetrahedral sites. The result is a ferrimagnetic material in which the net magnetic response can be attributed solely to the spin of the Fe^{2+} ions in the octahedral sites. Adapted from Kittel [8]

tribution to the magnetization of magnetite. The remaining eight Fe^{2+} ions occupy half of the 16 octahedral sites, and only their magnetic moments contribute to the net ferrimagnetic response [8]. This can be seen schematically in Fig 2.7. Ferrimagnets behave like ferromagnets in hysteresis response, but they have a lower saturation magnetization than would be expected from a pure ferromagnet.

Like ferromagnets, ferrimagnets exhibit long range magnetic order only at temperatures below a critical ordering (Curie) temperature. For magnetite, the Curie temperature is well above room temperature (858 K) [33]. As temperature is decreased below T_C, the saturation magnetization will increase following the Curie-Weiss law. This results in a saturation magnetization of 46 emu/g at 773 K [43], 92 emu/g at room temperature [8], and 90 emu/g at 15 K [44]. The anomalous decrease in the

saturation magnetization of magnetite in the low-temperature regime (< 120 K) is due to a structural transition which will be discussed in more detail in Chapter 4.

2.2.3 Antiferromagnetism

Antiferromagnetism is related to ferrimagnetism in that it requires two anti-parallel-aligned sublattices in a material. Antiferromagnetism occurs when the magnetic contributions from each sublattice is exactly equal, and consequently there is no net magnetization. This ordering occurs below a critical (Néel) temperature. As with ferromagnetic and ferrimagnetic materials, an external field is required to align the magnetic moments of the unpaired spins. The antiparrallel alignment of such a material will be along the direction of the externally applied field, similar to the alignment of ferromagnets and ferrimagnets.

Antiferromagnets are of special interest in this thesis because the electrodeposition studies herein show conditions for synthesizing, along with magnetite, other iron oxides and iron hydroxides. At least two of these materials, hematite (α-Fe_2O_3) and goethite (α-FeOOH), are antiferromagnetic and can be used with magnetite to elicit exchange anisotropy behaviour.

2.2.4 Exchange Anisotropy

Exchange anisotropy, also called exchange bias, was first discovered in 1957 by Meiklejohn and Bean while studying the magnetic properties of cobalt cooled to

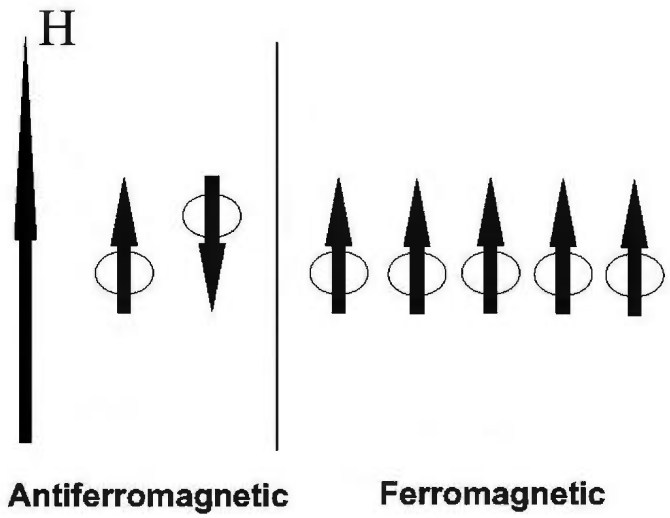

Figure 2.8: Schematic diagram of a system containing both ferromagnetic and antiferromagnetic materials under an applied magnetic field, H, and cooled/grown below the Néel temperature. Notice that the axis of magnetization is the same for both materials.

77 K in the presence of a strong magnetic field [45]. They noticed a unidirectional displacement of their hysteresis loops along the applied field axis. Upon further study, they found that this displacement was linked to the amount of cobalt oxide (CoO) formed on the surface of a compact of fine cobalt particles. They surmised that this effect was due to the ferromagnetic/antiferromagnetic interaction between the Co and CoO layers. Further study by Jacobs and Bean, and later by Néel, confirmed this interaction [46, 47]. They recognized that this interaction can be used to increase the coercive force of a material, similar to the way strain, crystalline anisotropy, and shape anisotropy had been used in the past.

Exchange bias requires an interface between antiferromagnetic and ferromagnetic

materials. In the simplest case, this interface is between two well-defined (often thin) layers of the two different materials. The application of a magnetic field will align the spins of the ferromagnet along the direction of the magnetic field, as is usual for a ferromagnet at temperatures below T_C. As the system is cooled or grown at temperatures below the Néel temperature of the antiferromagnet, the magnetic moments of the unpaired spins will align in the antiparallel order [48]. The spin alignment in the resultant layered system will be comparable to the schematic diagram in Figure 2.8. When the magnetic field is removed, ordering will remain in the direction of the applied field. Both the layers will still be aligned together, but it is important to note that the antiferromagnetic layer will contribute nothing to the saturation magnetization of this system. The result is a magnetization in one direction, as with a normal ferromagnet. If a magnetic field is now applied in the opposite direction of the original applied field, there will be a coercive anisotropy. Physically, this means the material will be easier to magnetize in one direction than in the other [49].

If this system is then subjected to a hysteresis study, a shifted loop will be found, as shown schematically in Figure 2.9. This exchange bias, named for the non-zero centering of the associated hysteresis loops, is due to the alignment of the antiferromagnetic magnetic moment pairs. The alignment of these pairs will "pin" the ferromagnetic layer in the direction of the original applied magnetic field [45, 46].

The exchange bias of a system is characterized by three coercive fields: H_{c1}, H_{c2},

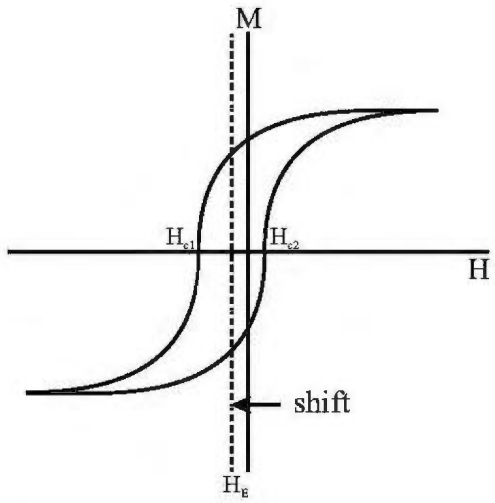

Figure 2.9: Schematic diagram of a schematic hysteresis loop displaying exchange bias. Notice the shift of the loop along the horizontal applied field (H) axis. The exchange field, H_E, is the average of coercivities H_{c1} and H_{c2}.

and H_E. The first two fields are the left and right coercive fields, and are defined by the applied field intercepts of a hysteresis loop. H_{c1} is of specific interest because it defines the magnitude of the applied field needed to flip the magnetization direction. H_E is the exchange bias field, which is the magnitude of the loop shift along the applied field axis [46].

In order to tailor magnetic response in exchange biased systems, there is much ongoing research in this field. Some of the current topics of interest include dynamic magnetic anisotropy at the onset of exchange bias [50], Monte Carlo simulations of iron-containing bilayers [51], non-applied field cooling induced exchange bias [52], exchange bias in dot arrays [53], and ferromagnetic/antiferromagnetic multilayers [54]. The materials used in these studies include [Pt/Co]-IrMn multilayers [55], Fe-

FeF_2 dot arrays [53], Fe/MnF_2 films [56], Pt/Co multilayers [52], FeF_2/Fe bilayers [51], and NiFe/IrMn layers [50].

Exchange anisotropy in magnetite-containing systems has not been extensively studied. Gatel *et al.* have studied the exchange anisotropy of Fe_3O_4/NiO bilayers grown epitaxially on single crystal MgO(001) and Al_2O_3(0001) in UHV conditions [57]. Del Bianco *et al.* have studied the exchange bias of iron nanoparticles embedded in a matrix of magnetite and maghemite [58]. Magnetite/cobalt oxide superlattices have been studied by Ijiri *et al.* [59]. The exchange bias caused by the oxidation of nanoparticles iron during annealing in an iron/nickel compact has also been studied recently [60].

Chapter 3

Experimental Methods

3.1 Synthesis

The electrodeposition of thin film magnetite involves a simple procedure using an electrolyte and a potentiostat/function generator/computer setup. The procedure uses some basic principles from electrochemistry along with some practical considerations.

3.1.1 Apparatus

The first consideration was the electrochemical cell, which was modified extensively throughout the first few months of use. This cell can be seen in Figure 3.1, and consists of a glass bottom and a Teflon top with seven holes to accommodate an Ag/AgCl reference electrode, working electrode, counter (auxiliary) electrode, two

argon purge tubes, a K-type thermocouple, and an external temperature probe. Comparable to ground in electronics, the reference electrode is used to measure the potential of the working electrode (WE). The reference electrode (RE) is a special type of electrode which maintains a constant potential under the small current that is needed to make electrochemical measurements. The working electrode (substrate) is the electrode at which the reaction of interest occurs, while a complimentary chemical reaction occurs at the counter (auxiliary) electrode (CE). A gold wire 2.1 mm thick was used as the counter electrode. Temperature control was maintained within $\pm 5°C$ with a Fisher Scientific Isotemp digital hotplate/stirrer with external temperature probe.

A galvanostat/potentiostat (Hokuto Denko HA 501, HA104) controlled the potential and current of the electrochemical cell in either of two modes. In potentiostatic mode, the potential between the reference electrode and the working electrode was controlled by regulating the current flow between the working electrode and the counter electrode. In galvanostatic mode, the current between the working electrode and the counter electrode was controlled by governing the potential between the working electrode and the reference electrode.

The analog current and potential data were digitized using a National Instruments BNC 2090 input connected to a National Instruments NI 6502E analog/digital converter board in a desktop PC. The data were recorded with a virtual instrument (VI) written in the National Instruments Labview 7.0 language by Bizzotto *et al.* [61] and

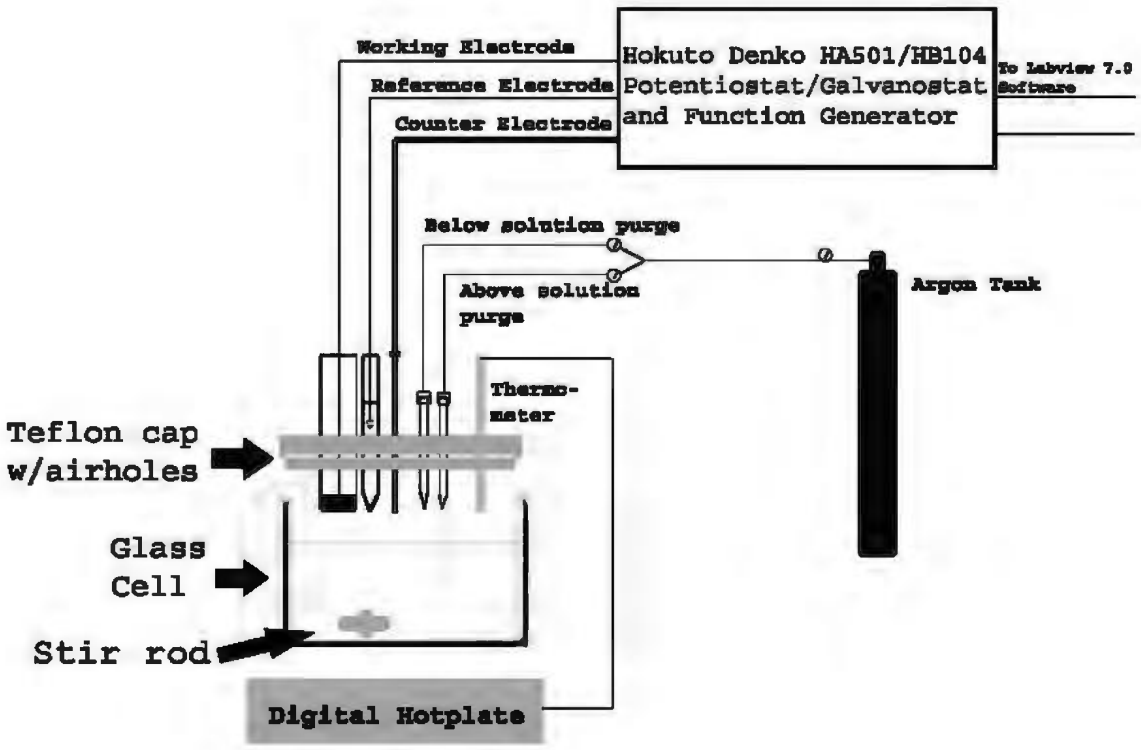

Figure 3.1: Schematic diagram of the setup used for the electrodeposition of magnetite during this thesis. This is a practical adaptation of a traditional setup, as described by Bard and Faulkner [20]

modified by the Poduska research group.

3.1.2 Procedure

Either polycrystalline brass or polycrystalline gold were used as the working electrode for the experiments reported here. The polycrystalline brass was common shimstock acquired from in-house supply storage. Due to the cold-rolling manufacturing technique, it had unidirectional striations. The polycrystalline gold (1250 Å, Erie Scientific) was vapour deposited on chromium (400 Å), which had been vapour deposited on glass slides. The flatness was < 40 μm deviation across the diagonal of a standard sized slide (25.10 ± 0.38 mm $\times$ 75.36 ± 0.38 mm).

Pretreatment was necessary to remove any contaminants present on the surface of the substrates. The brass shimstock was sanded, cut into disks, and dipped in concentrated (40%) HCl immediately before use, while the glass slides were cut into squares (7 mm $\times$ 7 mm) and kept in concentrated (96%) H_2SO_4.

Magnetite deposition was based on a procedure reported by Nishimura *et al.* [18] and later refined by Sorensen *et al.* [2]. The reaction is based upon the oxidation of Fe^{2+} ions at the surface of the working electrode, which occurs at -0.630 V *vs* SHE in solutions at pH 6.5 and near 80°C:

$$3Fe^{2+} + 4H_2O \rightleftharpoons Fe_3O_4 + 8H^+ + 2e^-. \tag{3.1}$$

When synthesized galvanostatically, magnetite was formed using a constant current

of either $50\mu A \cdot cm^{-2}$ or 88 $\mu A \cdot cm^{-2}$. Potentiostatic experiments were performed over a range of potentials from -0.200 V to -0.550 V.

A variety of electrolytes were utilized when forming thin films. Three different concentrations (0.04 M, 1.0 M, and 2.0 M) of potassium acetate (KCH_3COOH) were used in conjunction with iron salt (0.01 M $Fe(SO_4)_2(NH_4)_2 \cdot 6H_2O$). The pH values of these electrolytes were 6.0, 8.25, and 8.5 respectively. Electrolytes were prepared using ACS quality reagent salts purchased from EM Scientific, as well as nanopure water from a Barnstead Nanopure filter system (18.2 $M\Omega \cdot cm$).

The procedure for deposition was as follows. The working electrode, counter electrode, reference electrode, stirrer, and argon purge were all inserted into the electrolyte before heating. The counter electrode was kept in concentrated sulphuric acid beforehand in order to reduce the chance of contamination, and was rinsed before use. The cell was then heated to the desired temperature (70°C to 95°C) before any deposition was started. While heating the electrolyte, a cyclic voltammogram (CV) was recorded (-0.500 V to 0.100 V at 50 mV/s) to confirm the integrity of the electrical connection in the cell, and also to check for electrolyte or substrate contamination.

The iron salt was added to the solution after the target temperature was reached in order to reduce the formation of iron oxides and iron hydroxides prior to deposition. Monitoring was necessary during deposition because bubbles formed on the working electrode at high temperatures. Bubbles were removed using a jet of *in situ* electrolyte from a pipette. Deposition times of 10 to 90 minutes led to deposits on the order of

100 nm to 1000 nm in thickness. These thickness values were obtained by assuming the isotropy of crystallite dimensions and from weighing data. Due to the inherent uncertainty in these measurements, it is more helpful to use these measurements to confirm the order of magnitude of film thickness. After deposition, the sample was removed from the solution, rinsed with Nanopure water immediately, then dried with argon gas in order to reduce the formation of *ex situ* iron oxides and iron hydroxides.

3.2 Analysis Techniques

Various analysis techniques were performed on the electrodeposited thin films in order to extract information on phase identity, crystallite habit, crystallite size, lattice constants, deposit morphology, and magnetic hysteresis response.

3.2.1 X-Ray Diffraction

One of the main analytical techniques used in crystallographic characterization is X-Ray Diffraction (XRD), which can enable phase identification, lattice constant determination, and particle size estimations. The principles of XRD analysis can be explained using the Von Laue formulation of scattering [8, 62]. The Von Laue formulation assumes a crystal to be composed of many microscopic objects (atoms), placed on the sites $\mathbf{R}$ of a Bravais lattice. Each of these atoms reradiates in all directions the radiation incident upon them. From this system, sharp peaks will only

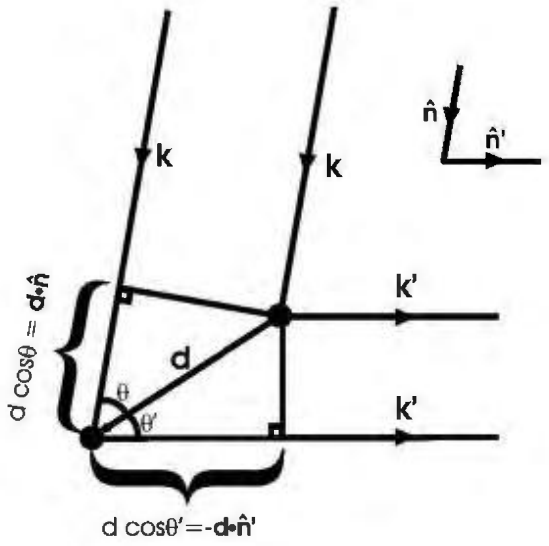

Figure 3.2: Schematic illustration of the Von Laue reradiator formulation. Adapted from Ashcroft and Mermin [62].

be seen at angles and wavelengths where constructive interference between scattered waves of neighbouring atoms occurs.

To satisfy the conditions for constructive interference, consider an X-ray of wavevector $\mathbf{k} = 2\pi\hat{\mathbf{n}}/\lambda$ incident upon two scatterers separated by a vector $\mathbf{d}$. Here, $\hat{\mathbf{n}}$ is the direction and λ the wavelength of the incident radiation. This geometry can be seen in Figure 3.2. The wavevector scattered from these particles can be described by the complimentary wavevector $\mathbf{k}' = 2\pi\hat{\mathbf{n}}'/\lambda$. The path difference between the two wavevectors is $\mathbf{d} \cdot (\hat{\mathbf{n}} - \hat{\mathbf{n}}')$. Constructive interference will occur when the path difference is an integral number of wavelengths:

$$\mathbf{d} \cdot (\mathbf{k} - \mathbf{k}') = 2\pi m, \tag{3.2}$$

where m in an integer. When applied to the complete Bravais lattice, this relation can be expressed as:

$$\mathbf{R} \cdot (\mathbf{k} - \mathbf{k}') = 2\pi m \tag{3.3}$$

Or equivalently:

$$e^{i(\mathbf{k}'-\mathbf{k})\cdot\mathbf{R}} = 1 \tag{3.4}$$

When this relation is compared with the characterization of the reciprocal lattice, the Laue formulation can be defined. The reciprocal lattice is defined by the set of wavevectors, $\mathbf{K}$, satisfying the relation $e^{i\mathbf{K}\cdot\mathbf{R}} = 1$. From this, the Laue condition states that constructive interference will occur provided that the change in wave vector, $\mathbf{K} = \mathbf{k}' - \mathbf{k}$, is a vector of the reciprocal lattice [62]. Consequently, any incident X-ray wavevector that satisfies this condition will satisfy the required constructive interference condition.

To do a complete analysis of a crystal structure, it is necessary to consider incident light over a range of wavevectors $\mathbf{k}$. This can easily be visualized using the geometric Ewald construction as shown in Figure 3.3. An incident wavevector $\mathbf{k}$ drawn in k-space with its origin on an atom, and a sphere (3D) or circle (2D) is drawn with its center at the tip of $\mathbf{k}$. There will be incident directions of $\mathbf{k}$ for which there exists a $\mathbf{k}'$ that satisfies the Laue condition. For the polycrystalline deposits studied in this thesis, grains of many different orientations are present. This ensures an isotropic

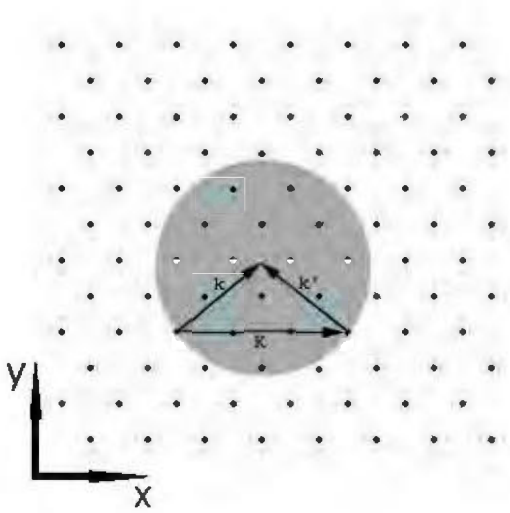

Figure 3.3: Two-dimensional representation of the Ewald construct sphere. The two vectors, $\mathbf{k}$ and $\mathbf{k}'$, satisfy the Laue condition and would lead to constructive interference. Adapted from Ashcroft and Mermin [62].

distribution of $\mathbf{K}$ over the Ewald construction sphere. By moving the X-ray source relative to the plane of the sample, all $\mathbf{k}'$ can be analyzed.

The equivalence of the Von Laue formulation with the Bragg formulation can be explained using Figure 3.4. The Bragg formulation relates the constructive interference of incident and scattered radiation to the the path difference of two rays reflecting from parallel atomic planes in a crystalline materials spaced a distance d apart. The incident and scattered rays, $\mathbf{k}$ and $\mathbf{k}'$, make the same angle θ with a plane perpendicular to $\mathbf{K}$, which allows the scattering to be viewed as Bragg reflection.

By definition, $\mathbf{K}$ is an integral multiple of the reciprocal lattice vector $\mathbf{K}_\circ$. Therefore the magnitude of $\mathbf{K}$ can be written:

$$K = nK_{\circ} = \frac{2\pi n}{d}. \tag{3.5}$$

Figure 3.4 also shows that $K = 2k\sin\theta$. When substituted into Eqn 3.5,

$$k\sin\theta = \frac{\pi n}{d}. \tag{3.6}$$

Since $k = 2\pi/\lambda$, we can see that Eqn 3.6 can be transformed into the Bragg reflection condition:

$$n\lambda = 2d\sin\theta. \tag{3.7}$$

To find the scattering angle due to a specific family of lattice planes, the unit cell dimensions are required. For cubic crystal structures, the spacing d depends on the cubic lattice constant a:

$$a = \frac{d^2}{h^2 + k^2 + l^2}. \tag{3.8}$$

XRD data for this thesis was collected on a Rigaku D/MAX 2200PC $\theta - \theta$ Powder Diffractometer. In its simplest form, an X-ray diffractometer is composed of three components: an X-ray source, a specimen, and a collector, as shown schematically in Figure 3.5. The X-ray source emits Cu-Kα (18 kV, 40 mA max) radiation at 1.5418 Å with a graphite monochromator. These X-ray photons reflect off of a specimen and are collected by a detector. The detector is typically a collection of

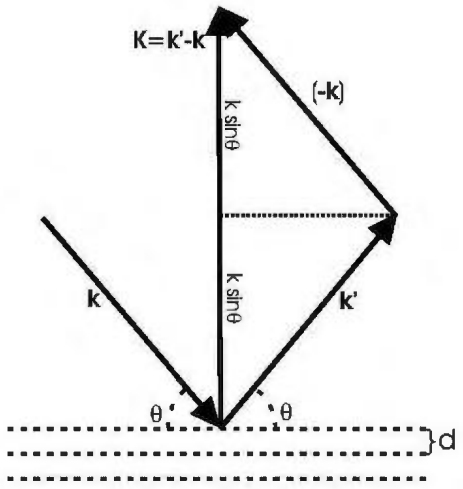

Figure 3.4: Diagram showing the equivalence of the Laue rereadiator formulation of X-ray scattering with reflection from a Bragg plane. The dashed line represents a Bragg plane perpendicular to **K**, **k**, and **k**′.

components, namely a beryllium window, a high linearity scintillation counter (such as a sodium iodide crystal), and a phototube. An X-ray photon that strikes the scintillation counter will excite an electron to a higher energy state, which then emits a photon as it returns to its ground state. The photon that is emitted is detected by a phototube, which relays this fact to a computer. The computer interface records the intensity and angle data for further analysis. In a $\theta - \theta$ diffractometer, both the collector and emitter and the collector move while the specimen is stationary. Consequently, the angle between the emitted and collector beam is 2θ. Bragg reflection from different families of lattice planes yields a plot of scattered X-ray intensity versus 2θ.

The diffraction patterns obtained in this thesis work were compared with data

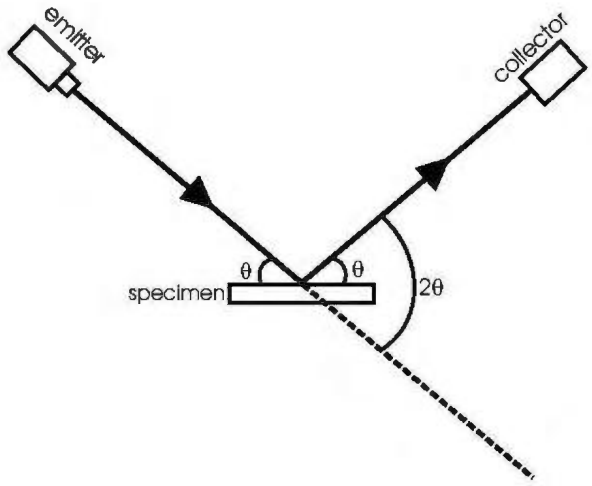

Figure 3.5: Diagram showing a typical X-ray diffractometer.

from the Joint Committee for Powder Diffraction Studies (JCPDS), a database of experimentally determined X-ray diffraction patterns of over 160,000 crystalline materials [63]. To confirm the presence of magnetite, or other phases of iron-containing compounds, the intensity and peak positions of experimentally collected data were compared against possible matches from the JCPDS database, such as the one for magnetite shown in Table 3.1. The peak positions and intensities are used to confirm the material identity, and possible preferred orientation. For example, a magnetite film that is made up of crystallites of predominantly (220) orientation should have a (220) peak intensity greater than the 26% that is seen in a randomly oriented sample [63]. Preferred orientation in a sample could be due to epitaxial growth, or other influences in deposit formation or preparation.

Table 3.1: Standard XRD diffraction pattern of magnetite, JCPDS #19 – 0629. Intensity is given as a percentage of the largest peak (311) [63].

2θ	Intensity (%)	(hkl)	2θ	Intensity	(hkl)
18.269	4	(1 1 1)	86.702	9	(6 4 2)
30.095	26	(2 2 0)	89.617	28	(7 3 1)
35.422	100	(3 1 1)	94.425	14	(8 0 0)
37.052	8	(2 2 2)	102.224	5	(6 6 0)
43.052	24	(4 0 0)	105.218	16	(7 5 1)
53.391	15	(4 2 2)	106.205	11	(6 6 2)
56.942	47	(5 1 1)	110.269	11	(8 4 0)
62.515	68	(4 4 0)	118.736	6	(6 6 4)
65.743	4	(5 3 1)	122.118	17	(9 3 1)
70.924	8	(6 2 0)	128.032	24	(8 4 4)
73.948	20	(5 3 3)	138.651	12	(10 2 0)
74.960	8	(6 2 2)	143.235	19	(9 5 1)
78.929	4	(4 4 4)	144.848	13	(10 2 2)

Lattice Constant Refinement

One of the critical tasks faced during this thesis work was the proper phase identification of deposited films. Because of the structural similarities between two iron oxide phases, maghemite ($\gamma-Fe_2O_3$) and magnetite (Fe_3O_4), qualitative inspection of the peak positions and intensities cannot distinguish definitively between the two phases. While the spacegroups of these two structures ($P4_132$ for maghemite and $Fd\bar{3}m$ for magnetite) are not overly similar, both materials have a cubic crystal structure with similar lattice constants (8.3515 Å and 8.3967 Å , respectively). This similar unit cell size leads to similar peak positions. For instance, the (311) peak of a cubic material with a lattice constant of 8.3967 Å (magnetite) is located at 35.422° 2θ, whereas the same peak for a cubic material with $a = 8.3515$ Å (maghemite) is lo-

cated at 35.630° 2θ. This difference is difficult to discern accurately by eye, so a quantitative least-square refinement of lattice constants based on peak positions is more informative.

Lattice parameter-refinement was performed using two freely-available programs. A Windows based program, Powder4 [64], was used in conjunction with the XRD data files to reduce noise using Savitsky-Golay smoothing, remove the background due to the plasticine used for mounting, and identify peak positions. The peak positions and intensities had to be verified manually since the automated routines are not perfect.

Secondly, the DOS based program, Prozski [65], was used as a front-end and organizer for various other crystallographic programs for lattice refinement. LATCON [66], a sub-program of Prozski, calculates the lattice parameters from user supplied peak positions using a simple non-iterative linear least squares fit of the data designed by D. Schwarzenbach *et al.* [67, 68]. Since the program suggests typically $5 - 10$ possible unit cells that fits one or all input peaks this program requires a great amount of user interaction.

Peak Broadening

Other useful information obtained from XRD data comes from measuring peak broadening. From the Scherrer formula, Eqn 3.9, it is easy to calculate the average crystal size.

$$t = \frac{0.9\lambda}{B\cos\theta_B} \tag{3.9}$$

Here, t is the average crystallite size, λ is the wavelength of the incident X-rays, B is the width of the peak at half maximum intensity in 2θ, and θ_B is the 2θ value for the peak in question. This technique was derived by Scherrer in 1918 to explain the broadening of peaks of crystallites $\sim$ 100 Å in diameter [69]. However, there are other contributing factors that influence the width of a diffraction peak. These include imprecise specimen displacement, non-flat or rough specimens, non parallel X-ray beam, or sample transparency.

3.2.2 Scanning Electron Microscopy

One of the two techniques that were used to analyze the morphology of deposited samples was scanning electron microscopy (SEM). SEM is a common imaging tool that employs the reflection of a beam of focused electrons off the surface of a sample [70]. A thermionic or field-emission cathode is typically used as the electron source for such a microscope. The beam of electrons are accelerated by a potential difference between the cathode and the sample/anode. The beam diameter is in the 10 nm range, which limits the magnification power of scanning electron microscopes.

A Hitachi S570 scanning electron microscope was used exclusively to produce micrographs for this thesis. The image is displayed on a video display in a raster scan that is synchronous with a scan across a sample, and captured photographically,

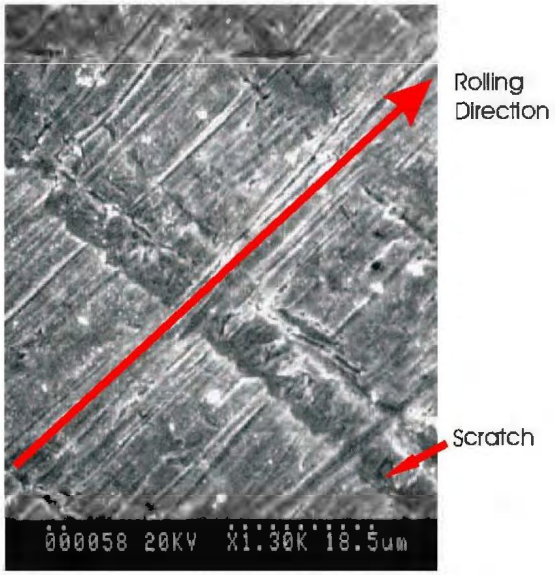

Figure 3.6: Scanning electron micrograph of the brass shimstock used as a substrate for the deposition of magnetite. The rolling direction is indicated in this image.

as shown in Figure 3.6. These images, while reminiscent of an aerial photo, do not necessarily provide an accurate topographical representation. The gradient of the grayscale is based on two main characteristics: atomic number and conduction. Materials that conduct better or have higher atomic numbers appear lighter, while less conducting or lower atomic number materials appear darker. Even though the conductivity of the films play an important role, atomic mass plays a greater role. The SEM micrographs were analyzed for crystallite homogeneity, crystallite size and habit. Magnification of 1000× to 30000×, corresponding to scans of 2 μm to 50μm respectively, were typically used for these analyses.

3.2.3 Energy Dispersive X-Ray Analysis

In conjunction with SEM, energy-dispersive X-ray (EDX) analysis was used to determine the elemental composition of electrodeposits. In particular, this technique was used to confirm the presence of iron in electrodeposited samples and to confirm the absence of contaminant elements. EDX systems are commonly incorporated into SEM instruments [70, 71]. An electron beam, the beam utilized by the SEM, is focused on a sample, and facilitates the release of an X-ray photon from a sample. The energy of the X-ray ejected is dependent upon the type of atoms in the sample. In a typical EDX spectrometer, this photon will then pass though a beryllium window onto a lithium-drifted silicon detector. This silicon detector is a *p-i-n* (*p*-type, intrinsic, *n*-type) semiconductor, reverse biased, and must be cooled with liquid nitrogen. The electron beam focused on the sample causes the ejection of an electron, and the creation of an electron-hole pair in the sample. The vacancy left by the ejected electron will be filled by an electron from a higher shell. To balance the energy loss of this electron, an X-ray will be emitted. The detector can determine the energy of the X-ray and the quanta of X-rays emitted from a sample. The data is then recorded and displayed by a computer system, and are compared against known X-ray energies for all elements. Data acquisition is very fast, usually requiring less than two minutes to collect enough data to clearly distinguish constituent elements. A Tracor Northern EDX was used in this thesis work, and an example of an EDX spectrum can be seen in Figure 3.7. With this particular system, it was not possible to identify atoms with atomic weights

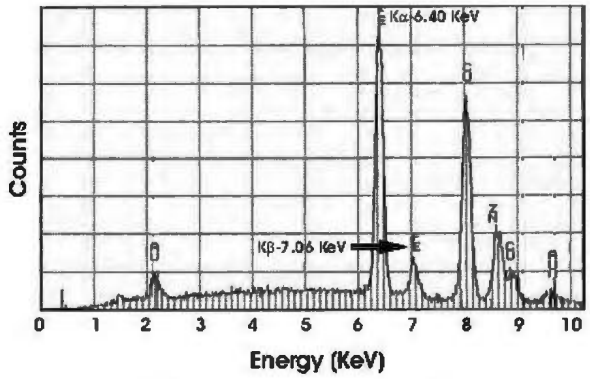

Figure 3.7: A representative energy dispersive X-ray (EDX) energy spectrum. Peaks from copper and zinc peaks in this spectra are due to the brass substrate, while gold peaks are due to the evaporated gold used to increase the conductivity of the films for SEM imaging. The iron peaks are due to the deposited magnetite. Oxygen is not seen here because its atomic number is too low to be detected by our system.

below that of sodium.

There are two main limitations of EDX that are of concern in the synthesis of iron oxides. The first is that it can not distinguish the ionic state of atoms, therefore can not distinguish between iron oxide phases.[1] Secondly, the data peaks are not weight-normalized and so do not directly show relative amounts of atoms in a sample. It is possible to do a semi-quantitative analysis of these peak area, but this is a process that requires a standard sample with a precisely known composition. Therefore, EDX was used only to qualitatively determine the elemental composition of samples, in order to detect any contamination of the magnetite thin films.

[1]X-ray photoelectron spectroscopy (XPS) can be used to distinguish the ionic state of Fe in different coordination environments. A preliminary XPS study of electrodeposited samples was undertaken but will not be described in this thesis.

3.2.4 Magnetometry

The magnetic response of electrodeposited thin magnetite films is one of the main interests of this thesis. A Quantum Designs MPMS SQUID (Superconducting Quantum Interference Device) magnetometer was utilized for the collection of most of the hysteresis data. To measure a magnetic response, a sample is placed within the magnetometer and subjected an applied magnetic field, **H**. This magnetic field is supplied by electromagnets driven by either alternating current (AC) imposed on a direct current (DC), or a direct current alone. To measure the effect that these magnetic fields have on samples, the magnetic response is detected by superconducting pickup coils, which experience an induced electric field caused by the changing magnetic field from the sample. In the DC method, the sample is either vibrated or translated to vary the magnetic field, while in the AC method, the fluctuations in the applied field induces an oscillating sample response which generates an electric field in the coil. A SQUID was used because the sensitivity of a SQUID is high enough to detect a magnetic field from weakly magnetized or thin samples.

Magnetization data were collected between 50 K and room temperature with a maximum applied field of 1000 Oe. Data collected with the on-site SQUID magnetometer were confirmed with data recorded with a similar device operated by Dr. T. Monchesky at Dalhousie University. Since room temperature hysteresis data was of primary interest, an attempt was made to use a magnetometer designed to measure the room temperature hysteresis response of ore samples. This magnetometer

utilized an applied magnetic field oscillating at 60 Hz and a copper pickup coil. Unfortunately, it was not sensitive enough to detect a signal from thin and small ($\sim 100\ \mu g$) electrodeposited samples.

3.2.5 Atomic Force Microscopy

Another powerful tool in the analysis of thin films is Atomic Force Microscopy (AFM), a type of scanning probe microscopy. The instrument used for AFM studies was a Asylum Research MFP3D, which allows different modes of scanned proximity probe microscopy. Both of these modes use a silicon cantilever to image samples. A laser is reflected off the back of the cantilever into a photodiode detector to detect changes in tip deflection as the tip is scanned across the surface of a sample. A feedback loop is used to adjust the height of the sample to maintain the force between the cantilever and the sample. This technique is done in a raster-scan pattern, and the resulting deflection information is displayed on a computer monitor.

The first type used in this thesis work utilized scanning force microscopy (SFM) with a silicon tip. This technique can be used to determine the morphology, homogeneity, and preferred crystal habit, similar to SEM micrographs. The advantage of an AFM is that it can also provide real height data, it can be performed in liquids, and it does not depend upon sample conductivity or elemental composition. However, rough surfaces are hard to image with an AFM because of the inability of the cantilever to adjust to large height jumps at high scan rates. This technique is also

slower and requires more training than for SEM operation. For instance, the collection time of an analog SEM micrograph is approximately two minutes, while the collection time for a 512 pixel $\times$ 512 pixel AFM image is approximately 25 minutes.

Another mode of operation mentioned in this thesis is Magnetic Force Microscopy (MFM). This technique uses a magnetized Co/Cr coated silicon tip of known magnetization direction to raster-scan a surface. The deflection of a cantilever equipped with a magnetized tip will be affected by the magnetic attraction or repulsion due to the interactions with a magnetized sample. This can allow the study of the domain structure of a material, including domain shape, size, and direction. Like AFM, excessive surface roughness can be detrimental to MFM studies. Both the SFM and MFM studies described here were performed in with an oscillating cantilever (AC-mode). MFM analysis will be mentioned further in Chapter 6.

Chapter 4

Influencing Morphology and Magnetism

In order to investigate the interplay between deposition conditions and magnetic properties of electrodeposited magnetite, several related studies were undertaken. The electrochemical synthesis of magnetite was explored and confirmed by comparing deposit structures (from X-ray diffraction data) with known structural characteristics of magnetite. The morphologies of magnetite electrodeposits were investigated in order to relate crystallite habit to deposition conditions. Finally, the morphology and synthesis conditions of electrodeposited films were correlated with changes in the magnetic hysteresis response.

4.1 Confirming Phase Composition

Magnetite electrodeposits were obtained using an electrolyte consisting of 0.04 M KCH_3COO + 0.01 M $Fe(SO_4)_2(NH_4)_2 \cdot 6H_2O$ (pH $\approx$ 6.5), which has been used by other groups to synthesize epitaxial magnetite thin films on single crystal gold [2]. Unless otherwise noted, this electrolyte will be considered the standard used in this thesis. Films were deposited potentiostatically on polycrystalline brass and gold substrates at potentials between -0.250 V and -0.450 V. Magnetite deposition was typically attempted for $10 - 90$ minutes at temperatures ranging from $70 - 90$°C.

The first step in confirming that magnetite deposition was occurring was the visual inspection of deposited films. Deposit colour is an important factor in determining phase identity because colour is indicative of different phases of iron oxides and iron hydroxides. Magnetite and γ-Fe_2O_3 (maghemite) are the two black iron oxide phases of interest, while α-Fe_2O_3 (hematite) and $\alpha-$FeOOH (goethite) are two reddish iron containing species of interest. At temperatures below 75°C, no deposit could be grown, while at temperatures above 85°C water evaporation caused bubbles to form on the working electrode disrupting the growth of the films. Black deposits were found at potentials ranging from -0.325 V to -0.450 V, while red films were deposited at more positive potentials (-0.250 V to -0.325 V). Films deposited between -0.325 V and -0.300 V were often a mixture of red and black deposits. Temperature was not a factor in the colour of deposited films.

X-ray diffraction (XRD) was utilized to confirm the presence of magnetite in

the deposited black films, and to identify any preferred crystallite orientation. The peak positions of experimental patterns were compared with known XRD patterns for magnetite, as shown in Figure 4.1. These XRD phase analyses showed that magnetite could be deposited over a 125 mV potential window (−0.325 V to −0.450 V). Lattice constant refinements using LATCON on three to six Bragg reflection peaks showed that the cubic lattice constant of these electrodeposited films was 8.396±0.009 Å. This value is in agreement with the accepted lattice constant of magnetite, 8.397 Å (JCPDS #19-0629) [63]. Additionally, all *hkl* reflections observed were allowed by magnetite's $Fd\bar{3}m$ spacegroup. It should be noted that XRD data confirmed the presence of magnetite in deposits prepared on both polycrystalline brass shimstock and (111)-textured Au/Cr/glass substrates. The XRD data were also inspected qualitatively for preferred orientation, by comparing the relative peak heights of experimental diffraction patterns with the relative peak heights of magnetite's standard diffraction pattern. However, overlap from deposit peaks and peaks from the substrate make a quantitative determination of preferred orientation difficult.

As mentioned in Chapter 3, galvanostatic methods were also utilized to synthesize magnetite. XRD analysis confirmed that magnetite could be deposited on brass and gold substrates at current densities between 50 $\mu A/cm^2$ and 88 $\mu A/cm^2$. A plot of potential versus time during a typical galvanostatic deposition can be seen in Figure 4.2. After an initial period of rapid current drift, the potential stabilizes to a value between −0.450 V and −0.325 V, where magnetite deposition occurs.

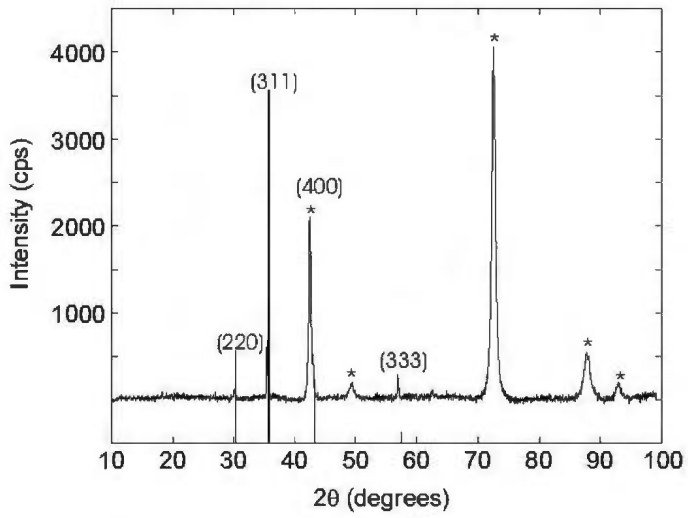

Figure 4.1: Indexed XRD diffraction pattern from a thin film of magnetite prepared by potentiostatic deposition at -0.375 V. Peaks resulting from the brass substrate are marked with an asterisk (*). The observed Bragg reflections are excellent matches with those expected for magnetite, JCPDS #19-0629 [63].

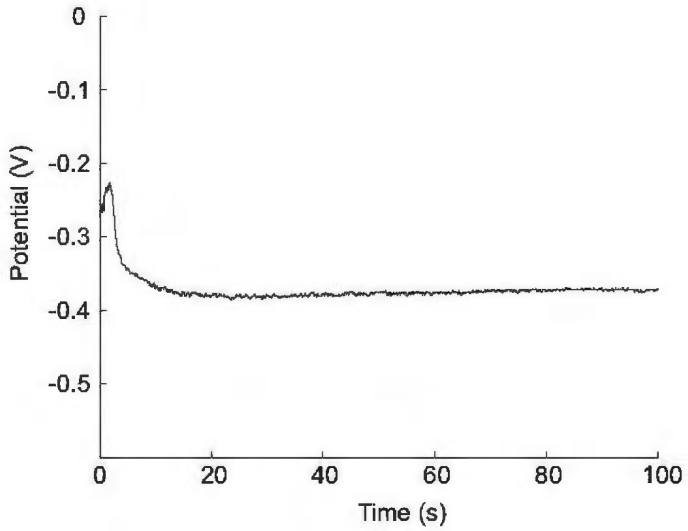

Figure 4.2: Applied deposition potential *vs.* time for a sample prepared galvanostatically at 50 μA/cm^2. Within the first 15 seconds of deposition, the applied potential stabilizes to a potential at which magnetite is electrodeposited, and no significant variation in potential is observed over $15 - 90$ minutes of deposition.

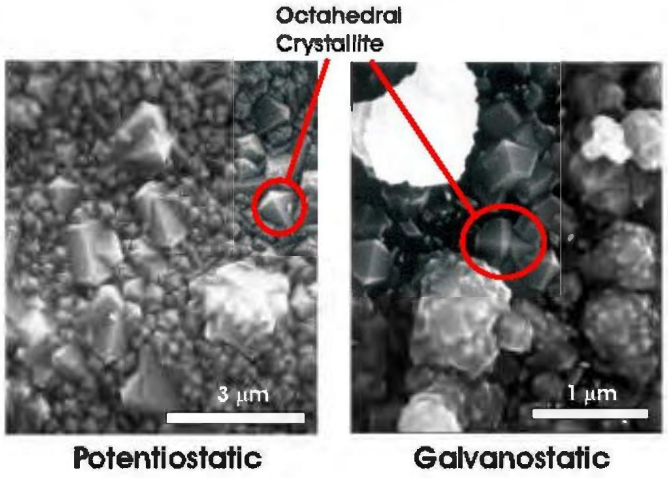

Figure 4.3: Scanning electron micrographs of magnetite deposited potentiostatically (-0.350 V for 30 minutes) and galvanostatically ($+50$ μA for 30 minutes). Octahedral crystallite habits, circled in red, are observed in samples prepared by either method. Energy dispersive X-ray analysis (EDX) was carried out on these samples in order to verify that no contaminants were present.

Scanning electron microscopy (SEM) showed that films, prepared either potentiostatically or galvanostatically, were comprised of crystallites with an octahedral habit for deposition times less than 30 minutes. Crystallites with this shape indicate faster growth along the $\langle 100 \rangle$ directions and slower growth along the $\langle 111 \rangle$ directions. Films that were deposited over longer periods, such as $0.5 - 1.0$ hours, formed faceted aggregate crystallites of the aforementioned octahedral habit, as shown in Figure 4.3.

As well as revealing crystallite morphology, SEM was also used to study the homogeneity and grain size of deposited films. SEM micrographs revealed films consisting of a bed of smaller (< 150 nm) crystallites with an even distribution of larger (> 200 nm) aggregate crystallites. Crystallite habit variations were consistent over the entire deposition area (0.4 cm^2), with an average crystallite size on the order of 100 nm esti-

mated by visual inspection of SEM micrographs. XRD peak broadening calculations suggest our deposits contain crystallite sizes in the range of $50 - 150$ nm. Studies by others in the field of magnetite electrodeposition do not address the issue of crystallite size directly, but magnetite crystallites with octahedral habits have been prepared by Peulon *et al.* on polycrystalline gold and synthesized from electrolytes containing NaCl, $FeCl_2$, and 1-methyl-imidazole [72]. Cubic crystallites were seen by Zhang *et al.* in magnetite electrodeposits prepared on polycrystalline substrates using an alternating current technique in an electrolyte containing iron sulfate and ammonium acetate [73]. Triangular prism crystallites have been observed for Fe_3O_4 electrodeposited on single crystal Au(111), Au(110), and Au(100) substrates by Nikiforov *et al.* [3].

4.2 Tuning Structure With Applied Potential

Outside of the potential region for magnetite deposition (-0.325 V to -0.450 V), other phases of iron oxide were deposited. XRD data from deposits prepared at -0.300 V to -0.325 V often indicated the presence of γ-Fe_2O_3 (maghemite). Lattice constant refinement on three to six Bragg reflection peaks yields a cubic lattice, with $a = 8.360 \pm 0.009$ Å which corresponds well with the cubic lattice constant for maghemite (8.3515 Å, JCPDS $\#39 - 1346$). At potentials more positive than -0.300 V, XRD data confirms the presence of goethite (α-FeOOH), a red material often used as a pigment [74]. Using LATCON for lattice refinement on six Bragg

reflection peaks, the orthorhombic lattice constants of the deposited goethite were found to be $a = 4.60 \pm 0.01$ Å, $b = 9.93 \pm 0.01$ Å and $c = 3.024 \pm 0.01$ Å, which is in agreement with the accepted values of $a = 4.608$ Å, $b = 9.956$ Å, and $c = 3.0215$ Å (JCPDS#29 – 013). Since maghemite and goethite contain only Fe^{3+} ions, whereas magnetite has a Fe^{2+}/Fe^{3+} ionic mixture, it is reasonable to find these phases at more positive (more oxidizing) potentials.

Linear sweep voltammetry was used to investigate the current response versus applied potential over the whole deposition range. The potential was swept from -0.550 V to -0.100 V at 1 mV/s and the current response was recorded, as shown in Figure 4.4. At potentials more negative than -0.450 V, this sweep displays a large cathodic current due to hydrogen evolution in the electrolyte. In the range linked with magnetite and maghemite deposition (-0.450 V to -0.300 V), the current response shows less noise than the current response seen at more positive potentials. At potentials above -0.300 V, a substantially more noisy current trace can be seen, which is consistent with deposits of the less electrically-conductive goethite. Linear sweep voltammetry was performed using both of the polycrystalline substrates, and there was no obvious difference between substrates.

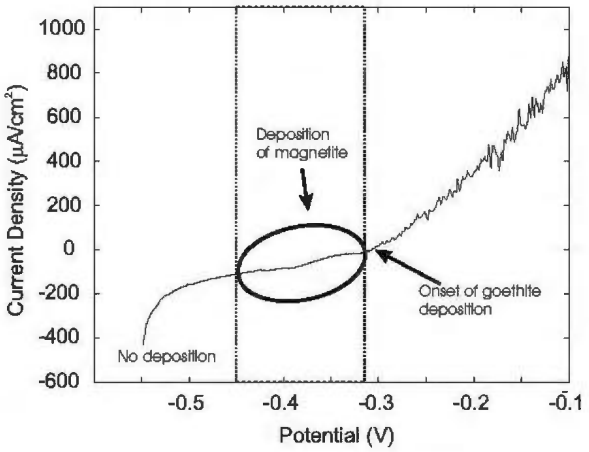

Figure 4.4: Linear sweep voltammogram of 0.01 M $Fe(SO_4)_2(NH_4)_2 \cdot 6H_2O$ + 0.04 M KCH_3COOH at 1 mV/s. The circled center region indicates the potentials at which magnetite can be deposited. In the region more negative than these potentials, no deposit is seen. In the region more positive than this, goethite (γ-FeOOH) forms.

4.3 Modifying Electrolyte to Affect Deposition Kinetics

The temperatures ($> 70°C$) required to deposit magnetite from aqueous electrolytes causes some practical problems with the deposition of magnetite. Bubbles that form at these temperatures can cause uneven film thicknesses across electrodeposited samples, and rapid evaporation of the electrolyte changes the electrolyte molarity during deposition. The studies outlined in the next two sections were attempted in order to reduce the temperature required for magnetite electrodeposition.

4.3.1 Ammonium Concentration

Previous studies of the affect of ammonium ions and the corresponding pH change on the formation of magnetite have shown interesting results with respect to deposition rate and temperature. During investigations into the effect of ammonia (NH_3) to change the pH of electrolytes for magnetite electrodeposition, Nishimura *et al.* found that the synthesis of magnetite occurred at its maximum rate for an ammonium ion concentration of 14.8 mM (pH = 7.5) at 80°C [18]. Above and below this concentration magnetite formed more slowly. They also found that the maximum rate of magnetite deposition at 24°C occurred with a lower concentration of ammonium, 11.8 mM (pH = 8.4). At both temperatures, magnetite formation slowed for ammonium concentrations higher and lower than optimum. In electrolytes with a pH greater than 8.4, this decrease in deposition rate was attributed to the formation of iron hydroxides such as $Fe(OH)_2$ and $Fe(OH)_3$ within solution.

The effect of ammonium (NH_4^+) ions was investigated on magnetite deposition by using 0.1 M ammonium acetate (NH_4CH_3COO) + 0.01 M ammonium iron sulfate (pH 6.7). Using this electrolyte increased the ratio of ammonium ions (0.12 M) to iron ions (0.01 M) relative to our standard electrolyte (0.02 M NH_4^+ to 0.01 M Fe^{2+}). This increase in ammonium allowed a change in the concentration of ionic species within the solution, without a substantial change in the pH of the electrolyte much (pH 6.7, compared to pH 6.5 for the standard electrolyte).

No magnetite films could be deposited from electrolytes with this drastically in-

creased ammonium concentration. At potentials more positive than −0.275 V, reddish films consistent in appearance with goethite were found, while at potentials more negative than −0.275 V, no films formed. At the other extreme, using an electrolyte with no ammonium ions (0.01 M $Fe(SO_4)\cdot 7H_2O$ + 0.04 M KCH_3COO, with pH 7), magnetite films were deposited successfully. Deposition rates using this electrolyte were comparable to those from the standard electrolyte. Consequently, very high levels of ammonium (relative to Fe^{2+}) suppressed the formation of magnetite, while a lack of ammonium was not detrimental to the formation of magnetite. *In situ* formation of iron hydroxide did not occur with either ammonium concentration because electrolyte pH was always below 8.4. Another cause could be the formation of *in situ* iron(II) ammonia complexes seen in high ammonium concentration solutions [75].

4.3.2 Acetate Concentration

A more successful attempt to reduce the temperature required for magnetite deposition involved using higher concentrations of potassium acetate, which serves as a complexing agent. When utilizing either 1.0 M or 2.0 M KCH_3COO along with 0.01 M $Fe(SO_4)_2(NH_4)_2 \cdot 6H_2O$, electrolyte pH increased to more basic values of 8.25 and 8.5, respectively. The upper potential limit for magnetite formation was shifted from −0.300 V (0.04 M acetate) to −0.375 V with the 1.0 M acetate. A shift to more negative potentials with increasing pH is predicted by the Nernst equation [19], but given the complexity of this system and the lack of buffering, a quantitative analy-

sis is not prudent. Qualitatively, it is easy to see that the change is pH shifted the potential window in the predicted direction. The potential window for magnetite is much larger (200 mV) for the increased acetate concentration, with a lower potential limit of −0.575 V.

One of the most startling differences between the standard and acetate-enriched electrolyte was the increased deposition rate. Samples deposited for ten minutes from the 1.0 M acetate electrolytes were of comparable thickness ($\sim$ 100 nm) as those deposited for 30 minutes from the 0.04 M acetate electrolytes. When the acetate concentration was increased to 2.0 M, the deposition rate did not continue to increase.

The potential windows for magnetite deposition from the 2.0 M acetate electrolytes (−0.425 V to −0.525 V) were comparable to that for the 0.04 M acetate solution: 100 mV, but shifted more negative due to pH. Maghemite formation sometimes occurred at the more positive end of this range (−0.425 V to −0.475 V). Red deposits, indicative of goethite, formed at potentials more positive than those for magnetite, while no deposits were formed at potentials more negative than −0.525 V.

The relation between acetate ion concentration and deposition temperature was also studied. Magnetite could be deposited at lower temperatures, as low as 60°C, with the 1.0 M and 2.0 M acetate solutions than with the 0.04 M acetate solution. The concentration of acetate was not increased above 2.0 M because such electrolytes would have a pH above 8.5, which would cause problematic *in situ* formation of iron

hydroxide.

Dramatic morphological differences were observed for samples deposited from acetate-enriched electrolytes. Rounded crystallites, as shown in Figure 4.5, were deposited over a potential range of −0.425 V to −0.550 V. These deposits were confirmed to be magnetite by XRD data, as shown in Figure 4.6, by comparison with the JCPDS powder diffraction file [63]. Lattice constant refinement performed on these samples found a lattice constant of 8.39 ± 0.02 Å, which is consistent with magnetite's accepted cubic lattice constant (8.3967 Å).

The results reported here indicate that an increase in acetate ion concentration is not detrimental to the formation of magnetite, but rather increases deposition rate. This increased deposition rate leads to more poorly formed, rounded crystallites. Data from ammonium and acetate concentration studies suggest that differences in deposition rate can be attributed largely to pH differences in the electrolytes. pH did increase with higher acetate concentrations, and shifted the potential deposition window in a manner consistent with the pH-potential phase stability of magnetite, as shown in Figure 2.2. A complete study would have included adjustments to keep the pH constant (through the addition of H_2SO_4 or KOH) while the supporting ion concentration was varied, but the intent of this section was to observe the general effect of both ammonium and acetate concentration on the electrodeposition of magnetite and so such a study was not completed.

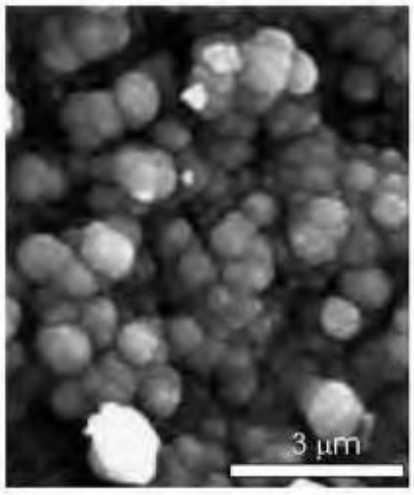

Figure 4.5: Scanning electron micrograph of magnetite deposited potentiostatically (−0.475 V for 25 minutes) from electrolyte containing 2.0 M acetate. More rounded crystallite habits are observed in samples prepared from electrolytes with higher acetate concentrations.

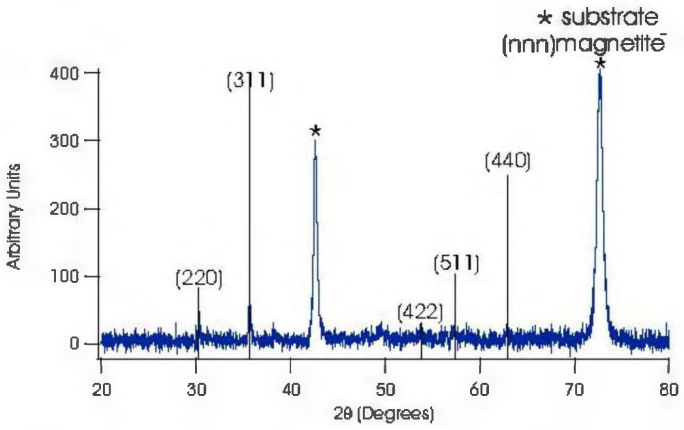

Figure 4.6: Indexed XRD diffraction pattern from a thin film of magnetite prepared by potentiostatic deposition at −0.475 V from an acetate-enriched electrolyte. Peaks resulting from the gold substrate are marked with an asterisk (*). The observed Bragg reflections are excellent matches with those expected for magnetite, JCPDS #19-0629 [63].

4.4 Magnetic Characterization

4.4.1 Verwey Transition

Magnetite undergoes an order/disorder transition when cooled below 120 K. This Verwey transition is characterized by a spontaneous lattice symmetry change coupled with an electrical conductivity change [40], and is due to an electronic change within the iron ion sublattices of magnetite. At temperatures above T_V, the Fe^{2+} valence electrons resonate between the 2+ ions and 3+ ions on the octahedral lattice sites, resulting in good electrical conduction ($\sim 0.01\ (\Omega cm)^{-1}$) [40, 76]. At temperatures below T_V there is a structural change (from cubic spacegroup $Fd\bar{3}m$ to monoclinic space group Cc), and therefore the Fe^{2+} valence electrons are not as free to conduct because they are more strongly bound to the Fe^{2+} ions [76]. For bulk magnetite, T_V is $120 - 125$ K [40, 77], but it can occur at lower temperatures for smaller particles (100 K) [78], in thin films (70 K) [79], or in strained films [80, 81].

Verwey transitions were confirmed in our electrodeposited samples by observing the magnetization versus temperature behaviour, as shown in 4.7. To observe this behaviour, the samples were cooled to 50 K in the absence of an applied field. Then an external magnetic field was applied as the sample was heated back to room temperature and the magnetization was measured (zero field cooled (ZFC) procedure). Then the sample was cooled to 50 K with the applied field present, and the magnetization was recorded as the sample was heated back to room temperature again

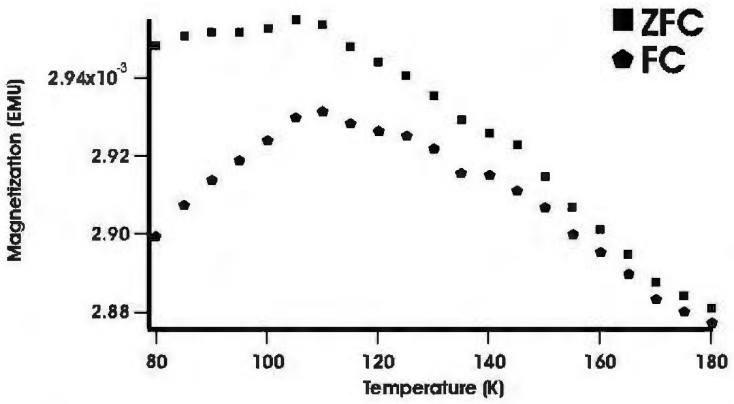

Figure 4.7: The temperature dependence of the saturation magnetization of a sample of electrodeposited magnetite (deposited potentiostatically at −0.375 V for 30 minutes). The magnetization was recorded after the sample was cooled both without a magnetic field (ZFC) and in a magnetic field (FC). The magnetization reaches a maximum at the Verwey temperature (115 K).

(field cooled (FC) procedure). A signature of the phase transition appears as a peak in magnetization at the Verwey temperature, T_V, near 115 K.

In this thesis, samples deposited in the potential range of −0.300 V to −0.450 V showed a Verwey transition near 115 K, slightly lower than that of bulk magnetite, as seen in Figure 4.7. The presence of a Verwey transition is known to be highly sensitive to impurities, with even very low levels leading to a complete suppression of the transition; magnetite with as little as 2.2% imputities has not shown a Verwey transition [82]. Therefore, the presence of a transition in electrodeposied samples is strongly indicative of high purity magnetite deposits.

4.4.2 Saturation Magnetization

Because saturation magnetization is an intrinsic property of a material, the saturation magnetization per mass is not expected to differ between samples. However, due to the low mass of electrodeposited samples ($\sim$ 100 μg) quantitative determinations of M_S proved to be difficult in these studies. The masses of the thin films were found by comparing the mass of the substrate and sample to the mass of the substrate alone, after dissolving the deposit in HCl. In many instances, the mass of water adsorbed from the air onto the samples was greater than the mass of the sample. To evaporate the surface adsorbed water, the samples were baked at $\approx 50°C$ for 25 minutes before weighing, in an attempt to reduce uncertainty to that associated with the microbalance (± 10 μg). Even after heating to reduce adsorbed water, saturation magnetizations in this thesis work were found to be suspiciously lower ($5 - 30$ emu/g) than the accepted theoretical value of 92 emu/g. Greatly reduced saturation magnetizations have been seen by Liu *et al.* in polycrystalline magnetite thin films ($5 - 1100$ nm) deposited by magnetron sputtering; for film thicknesses below 80 nm, saturation magnetizations were less than half the accepted value. This reduced saturation magnetization was attributed to an antiferromagnetic coupling between grain boundaries [83].

Given that XRD and temperature-dependent magnetization data provide strong evidence for the presence of magnetite in electrodeposited films, the discrepancies in saturation magnetization values are likely due to weighing inaccuracies or possible

grain boundary interactions. As a result, hysteresis loops in this thesis are displayed in terms of percent magnetization relative to saturation magnetization.

4.4.3 Hysteresis

In order to gain information about domain structure differences among magnetite electrodeposits, magnetic hysteresis behaviours, including coercivity and squareness, were studied. Hysteresis loops were taken on deposited films using either in-plane or perpendicular-to-plane applied magnetic fields, at 298 K, with a maximum applied field of 1000 Oe. Representative hysteresis data can be seen in Figure 4.8.

Hysteresis data show that there were no differences between in-plane or perpendicular-to-plane magnetic response in coercivity, squareness, or saturation magnetization. This suggests that the deposited films are magnetically bulk-like, even if they are on the order of 100 nm or less, and that there is no significant influence by the substrate on crystallite growth. SEM, XRD, and AFM results indicated that there were no substrate-dependent crystallite morphologies or crystallite orientations.

The electrodeposited magnetite samples from this thesis work displayed coercivities on the order of 100 Oe, which is consistent with the range of coercivities reported for magnetite films deposited by other methods. Coercivities for synthesized magnetite can be as low as tens of Oersted for thin films ($0.5 - 1.0$ μm) [73], or up to $\sim$ 600 Oe for thick films [84] or naturally occurring magnetite [34].

An interesting trend was observed between coercivity and deposition potential.

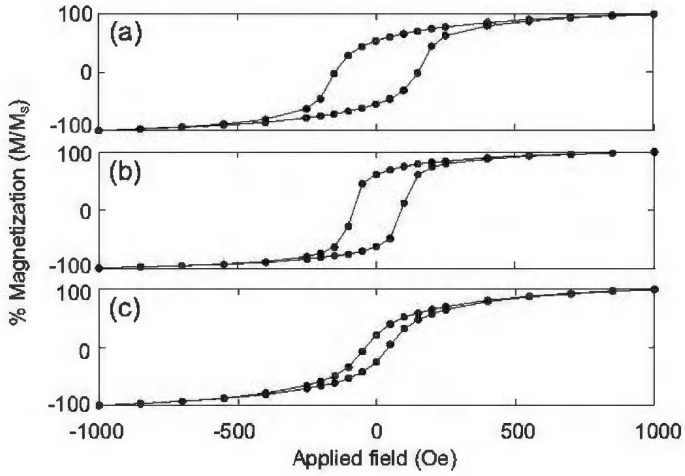

Figure 4.8: Representative magnetic hysteresis loops obtained from potentiostatically-deposited samples at −0.325 V (a), −0.350 V (b), and −0.425 V (c). The loops shown in (a) and (b) are from deposits prepared with electrolytes with 0.04 M acetate, while the loop in (c) is from a deposit prepared from an electrolyte containing 2 M acetate.

Figure 4.9 shows coercivity versus overpotential, which is the potential greater than the Nernst reversible potential for the Fe^{2+}/Fe^{3+} redox reaction (−0.630 vs. Ag/AgCl). Larger coercivities were seen at more positive overpotentials. This indicates that potential can be used to influence the domain structure of magnetite films. Lower coercivities signify the presence of smaller domain sizes in films deposited at lower overpotentials, while higher coercivities would indicate the presence of comparatively larger domains.

Squareness data, shown in Figure 4.10, underscore this link between overpotential and domain behaviour. Samples deposited in the standard solution at −0.375 V (overpotential of +0.196 V) had a squareness of 0.79±0.03 M_S. Squarenesses as low as ≈ 0.35 M_S were found in films deposited at at higher overpotentials (+0.246 V). The

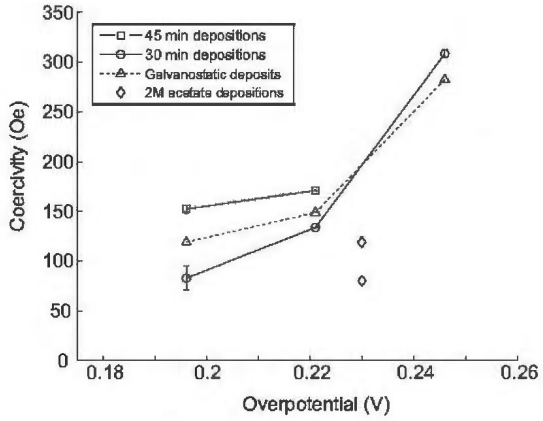

Figure 4.9: Magnetic coercivity plotted as a function of overpotential shows a strong trend of increasing coercivity with increasing overpotential. All coercivity data were obtained with a field applied in the in-plane orientation. The overpotentials are calculated relative to the pH-dependent Nernst reversible potential for the Fe^{2+}/Fe^{3+} redox reaction (-0.630 V *vs.* Ag/AgCl).

increase in squareness along with the decrease in coercivity (and *vice versa*) indicates that films deposited at lower overpotentials have pseudo-single magnetite domains while films formed at higher overpotentials are made of multi-domain crystallites. This trend suggests the domain behaviour, and hence coercivity, of magnetite can be altered with applied potential alone.

Electrolyte composition can have an even larger impact on the magnetite hysteresis response of magnetite deposits. Along with the morphological changes shown earlier, Figure 4.8(c) shows that the squarenesses of hysteresis loops of samples deposited using electrolytes containing 2.0 M acetate are much less than those of magnetite deposited from electrolytes containing 0.04 M acetate solution. The squareness of approximately 0.25 M_S and coercivity of $\sim$ 100 Oe is indicative of films composed

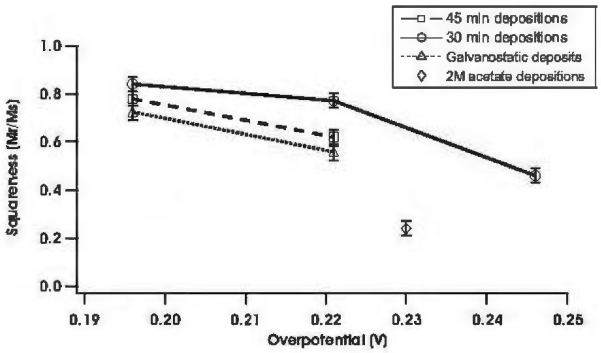

Figure 4.10: Hysteresis loop squareness plotted as a function of overpotential shows a strong trend of decreasing squareness with increasing overpotential. The overpotentials are calculated relative to the pH-dependent Nernst reversible potential for the Fe^{2+}/Fe^{3+} redox reaction (-0.630 V *vs.* Ag/AgCl).

of multi-domain crystallites. Thus, by changing the concentration of complexing agent, it is possible to synthesize magnetite films that display multi-domain crystallite behaviour.

Chapter 5

Electrodeposited Iron Oxide Composite Materials

5.1 Hysteresis Loop Shifts

While studying hysteresis data collected from magnetometry studies, it was evident that some hysteresis loops recorded at room temperature were shifted along the horizontal axis. This shift was found to be on the order of 10 Oe, or $\sim$ 10% of the coercivity of the samples, as shown in Figure 5.1. This shift was accentuated at temperatures near the Verwey transition (80–130 K).[1]

As mentioned in Section 2.2.4, a horizontal shift in hysteresis loops is indicative of an exchange bias between ferromagnetic and antiferromagnetic materials. This shift

[1]Samples for these temperature dependent studies were prepared by us and measured by Norman Deschamps and Dr. Ted Monchevsky at Dalhousie University

is due to a pinning of the ferromagnetic layer by the antiferromagnetic layer when the antiferromagnet/ferromagnetic system is cooled or grown below the Néel and Curie temperatures of the two materials, respectively. Another possible explanation for this shift is the constant instrument remanance field (± 10 Oe) associated with the magnetometers used to collect hysteresis data. However, the fact that the coercivity shifts were temperature dependent near the Verwey temperature suggests that the bias seen in the electrodeposited samples is not likely an instrument related artifact.

A review of the deposition procedure used in this thesis suggested a possible source of a multi-phase product that could lead to exchange bias behaviour. For some samples, the working electrode was held at 0 V for upwards of ten seconds while the iron salt was added to the solution. This applied potential would not lead to magnetite deposition, but rather an antiferromagnetic iron hydroxide, $\alpha-$FeOOH (goethite). This was confirmed by noting that very thin red films were sometimes left on the surface of the working electrode after dissolving the magnetite in HCl. Such deposits were too thin to yield appreciable XRD peaks. Films prepared while the potential was set to more negative, magnetite-forming potentials (-0.375 V) while the iron salt was added did not show evidence of exchange bias, nor were there red deposits remaining on the working electrode after magnetite dissolution. Therefore, under the former deposition conditions, it is possible to form a two-phase ferrimagnetic and antiferromagnetic deposit that could display exchange bias behaviour.

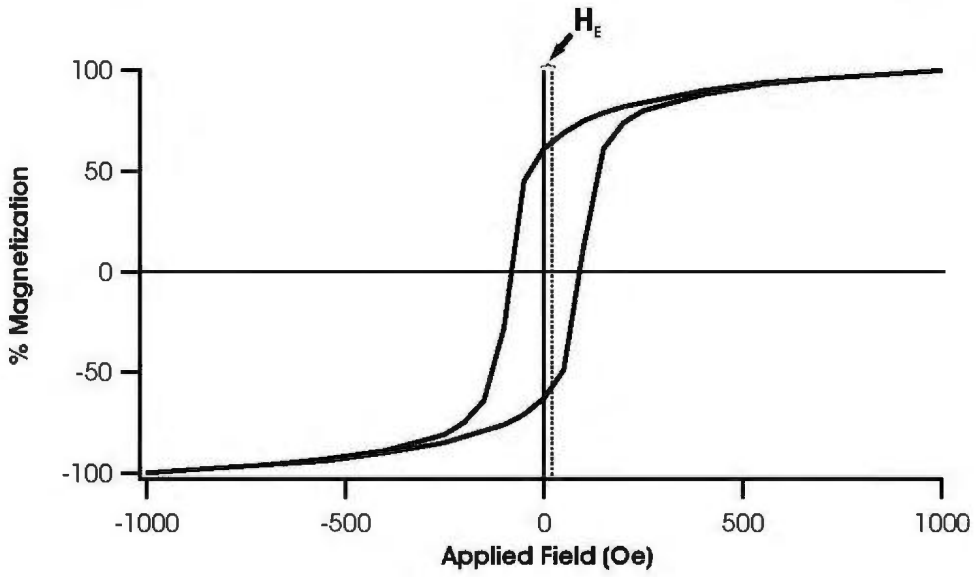

Figure 5.1: This hysteresis loop shows clear exchange bias with a positive shift along the x (applied field) axis of about 10%.

5.2 Preparation of Multi-Phase Deposits

In an attempt to intentionally create exchange biased electrodeposits, samples were prepared using a potential step technique, wherein the potential applied across the cell was stepped between values corresponding to the different deposition potentials of magnetite and goethite. Results presented in Chapter 4 show that magnetite forms at -0.375 V, and X-ray diffraction data from deposits prepared at -0.300 V confirm the presence of goethite only, as can be seen in Figure 5.2. The goal was to deposit distinct layers of each material.

An electrolyte containing 0.01 M $Fe(SO_4)_2(NH_4)_2 \cdot 6H_2O$ + 0.04 M KCH_3COOH, the standard electrolyte, was used to synthesize all deposits in these experiments.

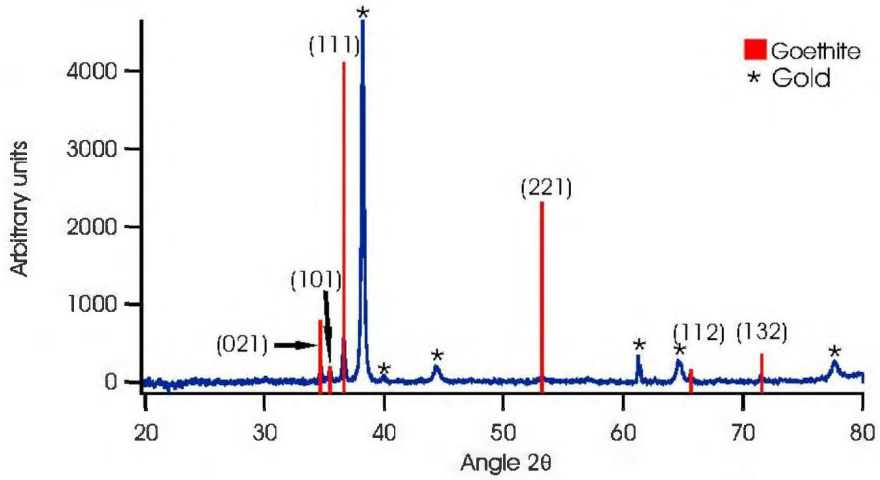

Figure 5.2: Indexed XRD pattern of a sample potentiostatically deposited at −0.300 V for 30 minutes. Peaks from the gold substrate are marked with an asterisk(*). This diffraction pattern is an excellent match with that of goethite (γ−FeOOH), JCPDS #29-0713 [63].

Deposition conditions are summarized in Table 5.1. The deposition time at −0.375 V (for magnetite formation) was kept constant throughout these experiments at 20 minutes, while the deposition time at −0.300 V (for goethite formation) was varied from 10 minutes to 15 seconds. The potential step sequence was also varied in an attempt to form the bilayer in either order.

X-ray diffraction data of these potential step samples confirmed the presence of both magnetite and goethite in all cases. However, visual inspection showed that most of the depositions did not yield distinct layers, but rather a mixture of reddish goethite and black magnetite. SEM micrographs, such as Figure 5.3, show the morphology of such two-phase film on the micrometer scale. In most samples, both phases were visible even though goethite was deposited first. The exception was when

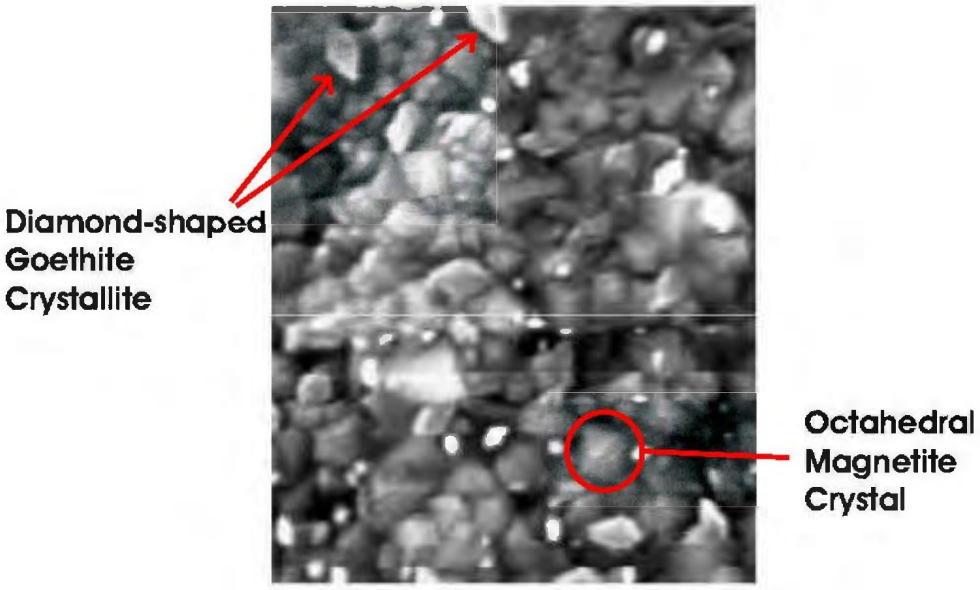

Figure 5.3: SEM micrograph displaying a mixed phase deposit where both goethite (diamond-shaped) and magnetite (octahedral) can be seen. This sample was prepared galvanostatically at 50 $\mu A/cm^2$ for 45 minutes.

the deposition of magnetite was attempted prior to the deposition of goethite. In this case, there was no visually obvious goethite deposit, yet XRD data confirmed the presence of this phase.

Due to circumstances beyond our control, magnetic hysteresis data of these samples has yet to be recorded. To reduce the possibility of false loop shifts due to instrumental remanent fields inside the magnetometer, these future measurements will involve quenching the magnet's remanence field to ≤ 0.5 Oe prior to each magnetization measurement at each applied field value. As soon as the instrumentation becomes available to perform these studies a fuller exploration will be made.

Table 5.1: Summary of deposition conditions for two-phase exchange biased samples. Goethite deposition occurred at -0.300 V (varying times), while magnetite deposition occurred at -0.375 V (20 minutes). The electrolyte, containing 0.01 M $Fe(SO_4)_2(NH_4)_2 \cdot 6H_2O$ + 0.04 M KCH_3COOH, and was maintained at 80°C.

Sample Number	Phase Deposited First	Length of Goethite Deposition (s)	Deposit Appearance
1	Goethite	600	Uniform reddish black mixture
2	Goethite	300	Uniform dark reddish black mixture
3	Magnetite	300	Uniform black
4	Goethite	180	Separate red and black sections
5	Goethite	60	Mostly black, reddish at center
6	Goethite	15	Uniform black

Chapter 6

Conclusions

6.1 Conclusions

Magnetite has shown promise as a material that could be utilized in the new age of microelectronic and spintronic applications, because it is a highly spin-polarized material with good conductivity and a wide operational temperature range. In order for magnetite to truly become a viable option for the manufacturers of spintronic devices, it must be cost efficient to synthesize it in high quality/high quantity forms that perform well in spintronic devices. This thesis work lays the groundwork for a complete characterization to discover whether electrodeposited magnetite is suited to these applications. This thesis describes the synthesis-structure-magnetic response relations of magnetite prepared by a cost efficient electrodeposition technique, and has found it suitable for extended studies into the spin-polarization and exchange

bias, both of which are important attributes for spintronic applications.

It was found that thin film magnetite can be electrodeposited on polycrystalline brass and gold substrates from an electrolyte with different iron:acetate ratios at temperatures between 75°C and 85°C. Potentiostatic deposition from standard electrolyte (acetate:iron ratio=4) yields magnetite over a relatively narrow potential range (150 mV), while galvanostatic formation of magnetite requires current densities ~ 40 $\mu A/cm^2$. The resulting magnetite films contained octahedral crystallites. Outside of these potential/current ranges, either different iron oxide phases formed (positive potentials) or no deposit formed (negative potentials).

Magnetic hysteresis studies showed that the deposition potential affects magnetic response. Magnetic coercivities increased monotonically and the squarenesses decreased with increasing overpotential. This suggests that samples prepared closer to magnetite's Nernst potential exhibit pseudo-single domain behaviour and multi-domain behaviour is displayed by samples prepared at higher overpotentials.

During experiments designed to reduce the deposition temperature, magnetite with a dramatically different magnetic response was formed. Using acetate-enriched electrolytes (acetate to Fe^{2+} ratios of $100-200$), magnetite was synthesized at temperatures as low as 60°C. However, the magnetite films deposited with these electrolytes also formed more rounded crystallites. This lead to drastically different magnetic coercivities (< 100 Oe) and squarenesses ($\approx 25\%$) relative to deposits prepared with the standard electrolyte. These magnetic responses also indicate that multi-domain

crystallites can be formed using these acetate-enriched electrolytes.

The dependence of ammonium concentration on magnetite deposition was investigated by utilizing electrolytes with ammonium:iron ratios of $0-10$. Results suggests that the presence of high levels of ammonium in solution blocks the formation of magnetite, perhaps by reducing the buffering ability of the acetate ions. Increased ammonia concentration has previously been linked with reduced magnetite formation through an associated increase in pH above 8.4 [18], but this is not the case in this study because the pH of the electrolyte used here was always below 8.4. The *in situ* formation of iron(II) ammonia complexes could also be the cause of this reduced magnetite formation [75].

Evidence of exchange anisotropy (of $\approx$ 10 % of H_C) was found during the electrodeposition of magnetite. Antiferromagnetic goethite is suspected to have been deposited in conjunction with magnetite on some samples, leading to a preliminary study of electrodeposited magnetite with an associated exchange bias due to the co-deposition of goethite. Early results in samples prepared to show intentional exchange bias have suggested that it is challenging to deposit well defined layers of the two materials. On-going studies in this area address the possibility of adjusting the magnitude of the exchnage bias by varying the relative amounts magnetite (ferrimagnetic) and goethite (antiferromagnetic) components within the deposit.

6.2 Future Studies

The work done in this thesis, while laying important groundwork to help understand synthesis–structure–property relations for electrodeposited magnetite, has also brought up some interesting questions that can stimulate further in-depth studies. Many of these issues relate to gaining a better understanding of crystallite growth during electrodeposition, assessing the spin-dependent electron transport of electrodeposited magnetite, or stem from the discovery of exchange bias within layers of electrodeposited magnetite. Many of the studies proposed here use an atomic force microscope as the main analysis tool, which is a recent addition to the capabilities of the Poduska Research Group laboratory.

Brillouin spectroscopy is one of the techniques that can be used to explore the spin-dependent properties of magnetite. Preliminary Brillouin studies, performed in conjunction with Dr. Todd Andrews, were undertaken on electrodeposited magnetite samples during the completion of this thesis. These studies have found the surface Raleigh wave velocity of the electrodeposited samples (3218 ± 98 ms^{-1}) to be consistent with the accepted value for magnetite (3200 ms^{-1}, [85]). Further study of magnon creation in magnetite is being planned. Magnon creation at temperatures approaching the Verwey temperature, in a variable applied magnetic field, and in films of varying thickness are some of the topics that could be covered in such a study.

In order to understand the magnetic domain structure of electrodeposited magnetite, it would be advantageous to study how magnetite crystallites nucleate and

grow. *In situ* (in electrolyte) atomic force microscopy would reveal how magnetite crystallites, and other iron oxide and hydroxide species, nucleate and grow on the surface of a substrate during electrodeposition. Before such a study can be conducted, some practical considerations must be addressed. Due to the small volume of the AFM-compatible electrochemical cells ($\approx$ 1 mL), the deposition temperature for magnetite must be reduced in order to combat evaporation problems/challenges. A solution must be also be found to suppress precipitate formation during the deposition of magnetite. In this thesis work, this suppression was achieved by de-gassing the electrolyte with argon. However, the bubbling of argon would be incredibly disruptive to AFM imaging. A proposed solution to this is the use of a flow through cell or a different electrolyte. If these obstacles were overcome, *in situ* AFM would be a powerful analysis technique for studying electrodeposited magnetite. This could be especially useful in studying the formation of goethite/magnetite composites described in Chapter 5.

Atomic force microscopy imaging of magnetite samples as they are dissolved in dilute acid could also provide data on the grain structure of electrodeposited samples. Such a study may not involve the problems of de-gassing, stirring, and heating, but would require a controllable way to ramp the pH of an aqueous solution without dissolving the sample too quickly, or saturating the solution so that the magnetite dissolution does not stop. By choosing an acid that dissolves magnetite and not goethite, or *vice versa*, this technique could also show the heterogeneity of species

and grain boundaries of a composite material. HCl, H_2SO_4, and HNO_3 all show promise in this regard because when composite samples are dissolved in these acids, a layer of reddish goethite is left behind.

A complete magnetic force microscopy (MFM) study of electrodeposited samples would also provide direct assessment of the domain structure ferromagnetic samples, as well as identify boundaries between phases in magnetite/goethite composite materials. Along with imaging across the top surface of a sample, MFM could also be performed on a cross section of magnetite to yield domain structure information as a function of thickness as well. A preliminary MFM study has been undertaken, but deposit roughness was too large to give meaningful MFM images. This deposit roughness problem must be solved before MFM experiments could supply any useful data. *In situ* (in electrolyte) MFM may also be possible, but signal to noise ratios are substantially reduced while imaging in fluid.

The surface magneto-optic Kerr effect (SMOKE) technique, which uses the change in polarization of a laser beam reflected off the surface of a magnetized sample (Kerr Effect) to probe the average magnetic properties of a thin film, could also be a possible technique to determine magnetic response of magnetite films. Along with providing magnetic response, this technique is less costly than SQUID magnetometry, requires less time, and can also provide spatially-resolved magnetic response. Unfortunately, this technique is limited in resolution to the width of the the laser source, which limits detection of the domain structure in electrodeposited magnetite samples.

Computer simulations could be beneficial to gain a better understanding of the role of exchange bias in samples containing both electrodeposited magnetite and antiferromagnetic iron-containing compounds. Micromagnetic modeling would be an appropriate approach because it considers the free energy (including magnetic anisotropy energy, ferromagnetic exchange energy, magnetoelastic energy, magnetostatic energy, and magnetic potential energy) of a material, and models magnetic domain structure and response to an applied field [86]. With this technique, the ferromagnetic/antiferromagnetic interfaces between magnetite and goethite could likely be modeled to link exchange bias seen during this thesis work with possible grain and domain arrangements.

Ultimately, the study of the magnetoresistance of electrodeposited magnetite samples is of interest when checking for the 100% spin-polarization desired for spintronic devices [87]. Sorenson *et al.* have found a spin-polarization of $\sim$ 40% in electrodeposited magnetite [2], even though magnetite ore is know to have 100% spin-polarization [88]. The standard four-terminal analysis method for magnetoresistance, where four terminals (two for current transfer and two to measure voltage) are attached to a thin film and the resistance is measured as a a function of applied magnetic field and temperature [89], could be used to test the magnetite samples electrodeposited here. This type of analysis could provide data on any relationship that may exist between deposition conditions/morphology and changes in the spin-polarization of electrodeposited magnetite. Preliminary investigations, using instru-

mentation in Dr. M. A. White's labratory at Dalhousie University, are in progress

While magnetite is a common and well known material, a complete characterization has yet to be performed that encompasses all its magnetite's properties. As new technologies (such as spintronic applications) and new techniques are invented and discovered, the existing data on many materials must be expanded to address their role in these new areas of science. Therefore, a study that considers magnetite's use as a spintronic device must be undertaken in order to more fully characterize this material. If the aforementioned studies could be completed, magnetite could prove to be very useful in microelectronic applications.

Bibliography

[1] Prinz, G. A. *Science* **1998,** *282,* 1660.

[2] Sorenson, T. A.; Morton, S. A.; Waddill, G. D.; Switzer, J. A. *Journal of the American Chemical Society* **2002,** *124,* 7604-7609.

[3] Nikiforov, M. P.; Vertegel, A. A.; Shumsky, M. G.; Switzer, J. A. *Advanced Materials* **2000,** *12,* 1351-1353.

[4] Zhang, Z.; Satpathy, S. *Physical Review B* **1991,** *44,* 13319-13331.

[5] Anisimov, V. I.; Elfimov, I. S. *Physical Review B* **1996,** *54,* 4387-4390.

[6] Mills, A. A. *Annals of Science* **2004,** *61,* 273-319.

[7] Abe, M.; Tamura, Y. *Japanese Journal of Applied Physics* **1983,** *22,* L511-L513.

[8] Kittel, C. *Introduction to Solid State Physics;* John Wiley and Sons Inc.: New York, Seventh ed.; 1996.

[9] Kennedy, R. J.; Stampe, P. A. *Journal of Physics D: Applied Physics* **1999,** *32,* 16-21.

[10] Dedkov, Y. S.; Fonin, M.; Vyalikh, D. V.; Hauch, J. O.; Molodtsov, S. L.; Rüdiger, U.; Güntherodt, G. *Physical Review B* **2004,** *70,* 073405.

[11] Wright, J. P.; Attfield, J. P.; Radaelli, P. G. *Physical Review Letters* **2001,** *87,* 266401.

[12] Margulies, D. T.; Parker, F. T.; Rudee, M. L.; Spada, F. E.; Chapman, J. N.; Aitchison, P. R.; Berkowitz, A. E. *Physical Review Letters* **1997,** *79,* 5162-5165.

[13] Therese, G. H. A.; Kamath, P. V. *Chemisty of Materials* **2000,** *12,* 1195-1204.

[14] Peulon, S.; Lincot, D. *Journal of the Electrochemical Society* **1998,** *145,* 864-874.

[15] Datta, M.; Landolt, D. *Electrochimica Acta* **2000,** *45,* 2535-58.

[16] Penner, R. M. *Journal of Physical Chemistry B - Condensed Phase* **2002,** *106,* 3339-53.

[17] Abe, M.; Tamaura, Y.; Oishi, M.; Saitoh, T.; Itoh, T.; Gomi, M. *IEEE Transactions On Magnetics* **1987,** *55,* 3432-3434.

[18] Nishimura, K.; Kitamoto, Y.; Abe, M. *IEEE Transactions On Magnetics* **1999,** *35,* 3043-3045.

[19] Wang, J. *Analytical Electrochemistry;* Wiley-VCH: New York, Second ed.; 2000.

[20] Bard, A. J.; Faulkner, L. R. *Electrochemical Methods: Fundamentals and Applications;* John Wiley and Sons Inc.: New York, Second ed.; 2001.

[21] Ives, D. J. G.; Janz, G. J. *Reference Electrodes: Theory and Practice;* Academic Press: New York, 1961.

[22] Petrucci, R. H.; Harwood, W. S. *General Chemistry: Principles and Modern Applications;* Macmillan Pubplishing Company: New York, Sixth ed.; 1989.

[23] Schöllhorn, R. *Angewandte Chemie International Edition English* **1980,** *19,* 983-1003.

[24] Switzer, J. A. *American Ceramic Society Bulletin* **1987,** *66,* 1521-24.

[25] Switzer, J. A.; Shane, M. J.; Phillips, R. J. *Science* **1990,** *247,* 444-446.

[26] Oh, C.-Y.; Oh, J.-H.; Ko, T. *IEEE Transactions On Magnetics* **2002,** *38,* 3018-3020.

[27] Hai, T. . H.; Van, H. T. B.; Phong, T. C.; Abe, M. *Physica - Section B* **2003,** *327,* 194-198.

[28] Switzer, J. A.; Liu, R.; Bohannan, E. W.; Ernst, F. *Journal of Physical Chemistry B - Condensed Phase* **2002,** *106,* 12369-12372.

[29] Pourbaix, M. *Atlas of Electrochemical Equilibria in Aqueous Solutions;* Pergamon Press: New York, 1966.

[30] Blundell, S. *Magnetism in Condensed Matter;* Oxford Masters Series in Condensed Matter Physics Oxford University Press: Oxford, 2001.

[31] Griffiths, D. J. *Introduction to Electrodynamics;* Prentice Hall: Upper Saddle River, Third ed.; 1999.

[32] O'handley, R. C. *Modern Magnetic Materials: Principles and Applications;* Wiley-Interscience: New York, 2000.

[33] Cullity, B. D. *Introduction to Magnetic Materials;* Addison-Wesley: Reading, Massachusetts, 1972.

[34] Hodych, J. P. *Earth and Planetary Science Letters* **1996,** *142,* 523-533.

[35] Szmaja, W. *Physica Status Solidi (a)* **2002,** *194,* 315-330.

[36] Medrano, C.; Schlenker, M.; Baruchel, J.; Espeso, J.; Miyamoto, Y. *Physical Review B* **1999,** *59,* 1185-1195.

[37] Ambatiello, A.; Fabian, K.; Hoffmann, V. *Physics of the Earth and Planetary Interiors* **1999,** *112,* 55-80.

[38] Pan, Q.; Pokhil, T. G.; Moskowitz, B. M. *Journal of Applied Physics* **2002,** *91,* 5945-5950.

[39] Pokhil, T. G.; Moskowitz, B. M. *Journal of Geophysical Research - Part B - Solid Earth* **1997,** *102,* 22681-94.

[40] Walz, F. *Journal of Physics: Condensed Matter* **2002,** *14,* R285-R340.

[41] Weiss, P.; Forrer, R. *Annals de Physique* **1929,** *10,* 279-374.

[42] Voogt, F. C.; Palstra, T. T. M.; Niesen, L.; Rogojanu, O. C.; James, M. A.; Hibma, T. *Physical Review B* **1998,** *57,* R8107-R8110.

[43] Dunlop, D. J. *Reports on Progress in Physics* **1990,** *53,* 707-792.

[44] Özdemir, Ö.; Dunlop, D. J.; Moskowitz, B. M. *Earth and Planetary Science Letters* **2002,** *194,* 343-358.

[45] Meiklejohn, W. H.; Bean, C. P. *Physical Review* **1957,** *105,* 904-913.

[46] Stamps, R. L. *Journal of Physics D: Applied Physics* **2000,** *33,* R247-R268.

[47] Jacobs, I. S.; Bean, C. P. *Magnetism: A Teatise on Modern Theory and Materials;* volume III Academic Press: New York, 1966.

[48] Noguès, J.; Leighton, C.; Schuller, I. K. *Physical Review B* **2000,** *61,* 1315-17.

[49] Craik, D. J.; Tebble, R. S. *Ferromagnetism and Ferromagnetic Domains;* volume IV of *Selected Topics in Solid State Physics* John Wiley and Sons Inc.: New York, 1965.

[50] McCord, J.; Mattheis, R.; Elefant, D. *Physical Review B* **2004,** *70,* 094420.

[51] Lederman, D.; Ramìrez, R.; Kiwi, M. *Physical Review B* **2004,** *70,* 184422.

[52] Sort, J.; Popa, A.; Rodmacq, B.; Dieny, B. *Physical Review B* **2004,** *70,* 174431.

[53] Eisenmenger, J.; Li, Z.-P.; Macedo, W. A. A.; Schuller, I. K. *Physical Review Letters* **2005,** *94,* 057203-1-4.

[54] Scholten, G.; Usadel, K. D.; Nowak, U. *Physical Review B* **2005,** *71,* 064413.

[55] Sort, J.; Baltz, V.; Garcia, F.; Rodmacq, B.; Dieny, B. *Physical Review B* **2005,** *71,* 054411.

[56] Macedo, W. A. A.; Sahoo, B.; Kuncser, V.; Eisenmenger, J.; Felner, I.; Noguès, J.; Liu, K.; Keune, W.; Schuller, I. K. *Physical Review B* **2004,** *70,* 224414.

[57] Gatel, C.; Snoeck, E.; Serin, V.; Fert, A. *The European Journal of Physics B* **2005,** *45,* 157-168.

[58] Bianco, L. D.; Fiorani, D.; Testa, A. M.; Bonetti, E.; Signorini, L. *Physical Review B* **2004,** *70,* 052401.

[59] Ijiri, Y.; Borchers, J. A.; Erwin, R. W.; Lee, S.-H.; van der Zaag, P. J.; Wolf, R. M. *Physical Review Letters* **1998,** *80,* 608-611.

[60] Löffler, J. F.; Meier, J. P.; Doudin, B.; Ansermet, J.-P.; Wagner, W. *Physical Review B* **1998,** *57,* 2915-2924.

[61] Bizzotto, D. World Wide Web: www.chem.ubc.ca/personnel/faculty/bizzotto/, Last accessed July 2005.

[62] Ashcroft, N. W.; Mermin, N. D. *Solid State Physics;* Brooks/Cole Thomas Learning: Austalia, 1976.

[63] Joint Commission on Powder Diffraction Standards – International Centre for Diffraction Data, "Powder Diffraction File", 2003.

[64] Dragoe, N. "Powder4 software", World Wide Web: http://www.ccp14.ac.uk/ccp/web-mirrors/ndragoe/, Last accessed July 2005.

[65] Lasocha, W.; Lewinski, K. "Prozski", World Wide Web, Last accessed Fall 2003.

[66] Schwarzenbach, D. "LATCON: Program for the LS-refinement of Lattice Constants", 1975.

[67] Schwarzenbach, D.; Abrahams, S. C.; Flack, H. D.; Gonschorek, W.; Hahn, T.; Huml, K.; Marsh, R. E.; Prince, E.; Robertson, B. E.; Wilson, J. S. R. A. J. C. *Acta Cryrstaollgraphica* **1989,** *A45,* 63-75.

[68] Schwarzenbach, D.; Abrahams, S. C.; Flack, H. D.; Prince, E.; Wilson, A. J. C. *Acta Cryrstaollgraphica* **1995,** *A51,* 565-569.

[69] Azaroff, L. V.; Buerger, M. J. *The Powder Method in X-ray Crystallography;* McGraw-Hill: New York, 1958.

[70] Goldstein, J. I.; Newbury, D. E.; Echlin, P.; Joy, D. C.; Fiori, C.; Lifshin, E. *Scanning Electron Microscopy and X-Ray Microanalysis: A Text for Biologists, Materials Scientists, and Geologists;* Plenum Press: New York, 1981.

[71] Reimer, L. *Scanning Electron Microscopy;* Springer Series in Optical Sciences Springer-Verlag: Berlin, 1985.

[72] Peulon, S.; Antony, H.; Legrand, L.; Chausse, A. *Electrochimica Acta* **2004,** *49,* 2891-2899.

[73] Zhang, Q.; Itoh, T.; Abe, M. *IEEE Transactions On Magnetics* **1994,** *30,* 4900-4902.

[74] Lemaire, B. J.; Davidson, P.; Ferré, J.; Jamet, J. P.; Panine, P.; Dozov, I.; Jolivet, J. P. *Physical Review Letters* **2002,** *88,* 125507-1-4.

[75] Mironov, V. E.; Pashkov, G. L.; Stupko, T. V.; Pavlovskaya, Z. A. *Russian Journal of Inorganic Chemistry* **1994,** *39,* 1611-1614.

[76] Tarnawski, Z.; Wiecheć, A.; Madej, M.; Nowak, D.; Owoc, D.; Król, G.; Kąkol, Z.; Kolwicz-Chodak, L.; Kozlowski, A.; Dawid, T. *Acta Physica Polonica A* **2004,** *106,* 771-775.

[77] García, J.; Subías, G. *Journal of Physics: Condensed Matter* **2004,** *16,* R145-R178.

[78] Poddar, P.; Fried, T.; Markovich, G.; Sharoni, A.; Katz, D.; Wizansky, T.; Millo, O. *Europhysics Letters* **2003,** *64,* 98-103.

[79] Zeise, M.; Blythe, H. *Journal of Physics: Condensed Matter* **2000,** *12,* 13-28.

[80] Lindley, R. A.; Sena, S. P.; Blythe, H. J.; Gehring, G. A. *Journal de Physique IV - France* **1997,** *7,* C1-617-618.

[81] Sena, S. P.; Lindley, R. A.; Blythe, H. J.; Sauer, C.; Al-Karafji, M.; Gehring, G. A. *Journal of Magnetism and Magnetic Materials* **1997,** *176,* 111-126.

[82] Yang, J. B.; Zhou, X. D.; Yelon, W. B.; James, W. J.; Cai, Q.; Gopalakrishnan, K. V.; Malik, S. K.; Sun, X. C.; Nikles, D. E. *Journal of Applied Physics* **2004,** *95,* 7540-42.

[83] Liu, H.; Jiang, E. Y.; Zheng, R. K.; Bai, H. L. *Physica Status Solidi (a)* **2004,** *201,* 739-744.

[84] Margulies, D. T.; Parker, F. T.; Spada, F. E.; Goldman, R. S.; Li, J.; Sinclair, R.; Berkowitz, A. E. *Physical Review B* **1996,** *53,* 9175-9187.

[85] Seikh, M. M.; Narayana, C.; Metcalf, P.; Honig, J.; Sood, A. K. *Phys. Rev. B* **2005,** *71,* 174106-1-6.

[86] Dahlberg, E. D.; Zhu, J.-G. *Physics Today* **1995,** 34-40.

[87] Wolf, S. A.; Awschalom, D. D.; Buhrman, R. A.; Daughton, J. M.; von Molnàr, S.; Roukes, M. L.; Chtchelkanova, A. Y.; Treger, D. M. *Science* **2001,** *294,* 1488-1495.

[88] Alvarado, S. F.; Eib, W.; Meier, F.; Pierce, D. T.; Sattler, K.; Siegmann, H. C.; Remeika, J. P. *Physical Review Letters* **1975,** *34,* 319-322.

[89] Cheetham, A. K.; Day, P. *Solid State Chemistry: Techniques;* Oxford University Press: Oxford, 1987.